HHS Public Access

Author manuscript

J Immunol. Author manuscript; available in PMC 2018 April 15.

Published in final edited form as:

J Immunol. 2017 April 15; 198(8): 3345–3364. doi:10.4049/jimmunol.1601291.

Systematic Analysis of Cell-Type Differences in the Epithelial Secretome Reveals Insights into the Pathogenesis of RSV-Induced Lower Respiratory Tract Infections

Yingxin Zhao[*,†,‡,1], **Mohammad Jamaluddin**[*,†,1], **Yueqing Zhang**[†], **Hong Sun**[†], **Teodora Ivanciuc**[§], **Roberto P. Garofalo**[*,‡,§], and **Allan R. Brasier**[*,†,‡]

[*]Institute for Translational Sciences, University of Texas Medical Branch, Galveston, TX77555

[†]Department of Internal Medicine, University of Texas Medical Branch, Galveston, TX77555

[‡]Sealy Center for Molecular Medicine, University of Texas Medical Branch, Galveston, TX77555

[§]Department of Pediatrics, University of Texas Medical Branch, Galveston, TX77555

Abstract

Lower respiratory tract infections (LRTIs) from Respiratory Syncytial Virus (RSV) are due, in part, to secreted signals from lower airway cells that modify immune response and trigger airway remodeling. To understand this process, we applied an unbiased quantitative proteomics analysis of the RSV-induced epithelial secretory response in cells representative of the trachea (hBECs) *vs* small airway bronchiolar cells (hSAECs). A workflow was established using telomerase-immortalized human epithelial cells that revealed highly reproducible cell type-specific differences in both secreted proteins and nanoparticles (exosomes). Approximately one-third of secretome proteins are exosomal, with the remainder from lysosomal and vacuolar compartments. We applied this workflow to three independently derived primary human cultures from trachea (phBECs) *vs* bronchioles (phSAECs). 577 differentially expressed proteins from control supernatants and 966 differentially expressed proteins from RSV-infected cell supernatants were identified at a 1% false discovery rate (FDR). Fifteen proteins unique to RSV-infected phBECs were regulated by epithelial-specific ets homology factor (EHF). 106 proteins unique to RSV-infected hSAECs were regulated by the transcription factor NFκB. In this latter group, we validated the differential expression of Chemokine (C-C Motif) Ligand 20 (CCL20)/macrophage-inducible protein (MIP)3α, thymic stromal lymphopoietin (TSLP) and chemokine (CC) ligand 3-like 1(CCL3-L1) because of their roles in Th2 polarization. CCL20/MIP3α was the most active mucin-inducing factor in the RSV-infected hSAEC secretome, and was differentially expressed in smaller airways in a mouse model of RSV infection. These studies provide insights into the complexity of innate

Address correspondence to: AR Brasier, MD, Department of Endocrinology, 301 University Blvd, Galveston, TX 77555-1060. arbrasie@utmb.edu.

[1]Equal first authors

Disclosures

The authors have no financial conflicts of interest.

Author contributions

YXZ, MJ YQZ, HS and TI performed experiments. YXZ, RPG and ARB conceived and designed experiments. YXZ, MJ YQZ, HS, TI, RPG and ARB interpreted experiments. YXZ and ARB wrote the manuscript. All authors approved the final submitted manuscript.

responses, and regional differences in epithelial secretome participating in RSV LRTI-induced airway remodeling.

Keywords

Airway Epithelial Cells; label-free proteomics; Chemokine (C-C Motif) Ligand 20 (CCL20); macrophage-inducible protein (MIP)3α; Thymic Stromal Lymphopoietin

Introduction

Human Respiratory Syncytial Virus (RSV) is a ubiquitous paramyxovirus pathogen that infects virtually all children by the age of 3, causing significant morbidity (1, 2). The presence of RSV infection produces 3-times the risk of subsequent hospitalization over that seen in infections with other common cold viruses, and hospitalization rates as high as of 17 per 1000 cases are seen in prospective epidemiological studies on young children (3).

RSV infections produce a variety of clinical syndromes including upper respiratory tract infections (with or without recurrent otitis media) and lower respiratory tract infections [LRTIs (1, 4)]. Although the majority of infections produce an uncomplicated URI, in ~2% of predisposed children RSV can spread into the lower airways, producing LRTI (1, 5, 6). RSV is consequently the most common cause of childhood LRTIs (7), responsible for 120,000 hospitalizations for LRTI (bronchiolitis) in the US annually (8), and represents the leading cause of infant viral death worldwide (9). Apart from its acute morbidity, severe LRTIs are associated with reshaping the pulmonary immune response, producing Th2 polarization and enhancing susceptibility to recurrent virus-induced wheezing through the next several decades of life (10). The mechanisms by which LRTIs reprogram the pulmonary immune system are not fully understood.

As a mucosa-restricted virus, in natural infections RSV initially replicates in the epithelium of the nasopharynx. In immunologically naïve infants, RSV spreads by cell-cell transfer and extracellular binding, producing discontinuous foci of infection in the tracheal epithelium (11). Further spread of RSV infection to distal bronchioles and the alveolar epithelium induces necrosis and sloughing. Sloughed epithelial cells are encased in fibrin and mucin, producing a ball-valve obstruction and ventilation-perfusion mismatching, impairing gas exchange and causing hypoxia, one of the most significant clinical features of LRTIs. The mechanism by which RSV produces epithelial sloughing has recently been partly elucidated: the intracellular expression of RSV nonstructural (NS) protein NS2 disrupts ciliary tubulin IV, obliterating epithelial ciliary function and inducing detachment from the basal lamina (12).

Because RSV LRTI occurs in immunologically naïve infants, the innate immune response plays an initiating role in LRTI pathogenesis. It has been extensively demonstrated that RSV replication in epithelial cells triggers a coordinated global genomic response that results in epithelial secretion of mucins, defensins, antiviral cytokines and proinflammatory chemokines that coordinate inflammation and adaptive immunity (13–15). Enhanced activation of innate inflammation has been demonstrated in children with bronchiolitis,

where enhanced expression of IL-6, -8 and MIP-1β have been observed (16). Important to the pathogenesis of LRTI, the epithelium in the proximal conductive airways and the respiratory surface play functionally distinct roles in innate defenses (17, 18). Under normal conditions, inhaled pathogens are cleared via the mucociliary escalator from ciliated epithelial cells. This defense is coordinated with the actions of the airway lining fluid, rich in antioxidants, defensins, and lysozyme secreted by clara cells and submucosal glands and that of mucous glycoprotein secreted by goblet cells (19). When these conductive epithelial cells are infected with RSV, they secrete CXCL chemokines macrophage inhibitory protein (MIP)-1 and type I/III interferons (IFNs). These latter cytokines activate resident plasmacytoid dendritic cells (DCs) to upregulate CD-40, -80 and -86 co-stimulatory molecules, inducing their migration to draining lymph nodes to stimulate cytotoxic T lymphocytes, which include natural killer and CD4/8+ memory T cells (17).

By contrast, when nonciliated epithelial cells located in the conductive airways (terminal bronchioles and alveoli) are infected with RSV, they express the CCL-type cytokines (TARC, MCP-1, and MDC), type I/III IFNs, and surfactants (15). These factors activate alveolar macrophages and pulmonary DCs (pDCs) to induce neutrophil recruitment and promote macrophage survival. Gene profiling experiments have suggested that these CCL-type chemokines are produced to a greater degree than by epithelial cells of the conducting airways (20). These findings suggest the presence of distinct regional, cell type-specific differences between activated conductive vs respiratory epithelial cells that may be immunologically important (15, 20). Despite this knowledge, there has been no systematic analysis of secreted proteins that would provide an understanding of the distinct mechanisms of innate immunity in different regions of the pulmonary tree.

To address this deficiency, we undertook a systematic analysis of RSV-induced secreted proteins in two principal cell types of the airways – bronchial epithelial cells (hBECs), derived from the trachea and representing the conducting portion of the airway, *vs* nonciliated small airway epithelial cells (hSAECs), representing nonciliated cells from terminal bronchioles that play a role in lower airway obstruction in RSV LRTIs (21). We first standardized a workflow by analysis of control and RSV-induced conditioned medium (CM) in telomerase (Tert)-immortalized hSAECs and hBECs, using quantitative label-free mass spectrometry. Our analysis was highly reproducible and identified distinct patterns of induced and inhibited proteins. Interestingly, exosomes constituted a significant fraction of the secretome; their protein contents also differed by cell type and were affected by RSV infection. We extended this workflow to analyze multiple non-immortalized primary cells from independent donors. Strikingly, hSAECs showed enhanced expression of immunologically important chemokines – CCL20/MIP3α, TSLP and CCL3-L1. We demonstrate that CCL20/MIP3α is the most active mucin-inducing factor in RSV CM from hSAECs, and discuss the implications of regional differences in the epithelial secretome for the pathogenesis of LRTIs.

Materials and Methods

Cell culture and treatment

Immortalized human bronchial epithelial cells (tert-hBECs) and small airway epithelial cells (tert-hSAECs) were established by transducing primary cells with human telomerase and cyclin- dependent kinase (CDK)-4 retrovirus constructs (22, 23). hBECs and hSAECs were grown in basal medium supplemented with growth factors (Lonza, Walkersville) in 10 cm Petri dishes in a humidified incubator with 95% air/5% CO_2 at 37 °C. At 80–90% confluence, the medium was changed, fresh basal medium without growth supplements was added to the plates, and the cells infected with pRSV (MOI 1.0) for 24h. Conditioned Medium (CM) was collected and centrifuged at 2000 x g at 4 °C for 20 min to remove any dead cells. The supernatant was centrifuged at 10,000 x g at 4 °C for 10 min to remove any cell debris. The supernatant was used immediately for secretome analysis. Cells from the same plates were lysed in Trizol for whole- cell protein preparation. Experiments were performed in biological triplicates.

For studies with primary human bronchial epithelial cells (phBECs) and phSAECs, cells from three different donors were obtained from Lonza (Supplemental Table I). CM was prepared from hBECs or hSAECs 24 h post-infection (MOI=1.0). When indicated, CM for UV-inactivated RSV-infected cells was used to stimulate hBECs at a 1–25% (vol/vol) concentration for the indicated times. UV inactivation was as previously described (24). For antibody neutralization, 20 μL of RSV-CM was mixed with anti-CCL20 Ab (R&D Systems, Minneapolis, MN).

Exosome preparation

Exosome isolation was performed by differential centrifugation at +4 °C to minimize protein degradation. Cells were removed by low-speed centrifugation at 400 x g, 10 min. The cleared supernatant was then sequentially centrifuged at 2000 x g for 15 min and 10,000 x g for 30 min to remove any remaining cell debris/microvesicles. Exosomes were finally pelleted by ultracentrifugation at 100,000 x g for 2 h and washed in PBS (without Ca++ or Mg++) at 100,000 x g, 60 min. After washing, the pellet was resuspended in a total of 200 μL of PBS. Exosome size was estimated by dynamic light scattering using a Malvern High-Performance Particle Sizer (Malvern Instruments, Westborough MA). Data acquisition and analysis were performed using Dispersion Technology Software (DTS, V4.1.26.0) configured for HPPS analysis. Each experimental group had three independent replicates.

Preparation of sucrose cushion-purified RSV (pRSV)

The human RSV A2 strain was grown in Hep-2 cells and prepared by sucrose cushion centrifugation as described (50). The viral titer was determined by a methylcellulose plaque assay. pRSV aliquots were quick-frozen in dry ice-ethanol, and stored at −70 °C until use.

Immunofluorescence (IF) microscopy

Airway cells were plated on cover glasses pretreated with rat tail collagen (Roche Applied Sciences). The cells were fixed with 4 % paraformaldehyde in PBS, permeabilized with 0.1% Triton X-100, blocked in 10% goat serum, and incubated with primary rabbit

polyclonal Ab to cytokeratin-7 or 19 as indicated (25, 26). After incubation with Alexa-goat anti-Rb Ab, cells were washed and counterstained with 4′,6-diamidino-2-phenylindole (DAPI). The cells were visualized with a Zeiss fluorescence LSM510 confocal microscope at 63x magnification.

IF of paraffin-embedded mouse lung was performed following standard protocols. Briefly, lung sections (5-μm) were deparaffinized in xylene and hydrated in ethanol (100% – 70%). Sections were washed with deionized water. Antigen unmasking was done with 1.0 mM EDTA, pH8.0. Sections were washed in H_2O and blocked with 10% goat serum for 1 h at room temperature in the dark, followed by primary antibody against CCL20 (1:200 dilution, Abcam) overnight at 4 °C in the dark. Sections were washed with TBS-Tween (0.1%) buffer and incubated with goat secondary Ab conjugated with Alexa 568 (DAKO) for 1h at room temperature in the dark. Sections were washed in TBS-Tween (0.1%), incubated with DAPI for 1 min, mounted on coverslips and visualized by confocal microscopy (Zeiss) and photographed at 63x magnification.

Apoptosis assay

Apoptosis was measured using a commercial annexin V-FITC apoptosis detection kit following the manufacturer's protocol (BioVision, Milpitas, CA). Briefly, hBEC and hSAEC cells ($1x10^6$) were infected with or without RSV (MOI 1.0) for 24h. Cells were dislodged with Accutase (Millipore), washed once with PBS and incubated with 5 μL of annexin V-FITC and 5 μL of Propidium Iodide (PI) in 500 μL of binding buffer for 5 min at room temperature in the dark. Annexin V-FITC and PI labeling was measured by flow cytometry.

Transmission Electron Microscopy (TEM)

A 10 μL aliquot from the exosome suspension was diluted in deionized water, applied to 200 mesh Formvar/carbon coated copper grids (Electron Microscopy Sciences) for 10 min at room temperature (24 °C) and negatively stained with 2% uranyl acetate (UA). The grids were examined in a Philips CM-100 transmission electron microscope at 60 kV FEI (Thermo-Fischer). Exosome images were acquired with a Gatan Orius 2001 charge-coupled device (CCD) camera.

Secretome digestion

About 10 mL of the CM supernatant was added into a 3K filter unit (Millipore, Billerica, MA) and centrifuged at 14,000 x g for 15 min. 400 μL of 8 M urea was added into the filter unit and centrifuged at 14,000 x g for 15 min, and this step repeated once. The solution remaining in the filter device was collected for protein digestion. Proteins were reduced with 10 mM dithiothreitol for 30 min, followed by alkylation with 30 mM iodoacetamide for 60 min in the dark. The sample was diluted 1:1 with 50 mM ammonium bicarbonate. Proteins were digested with 1.0 μg LysC-tr (Promega) for 12 h at 37 °C and then diluted 4:1 with 50 mM ammonium bicarbonate. The proteins were further digested with 1.0 μg trypsin (Promega) for 16 h at 37 °C. The digestion was stopped with 0.5 % trifluoracetic acid (TFA) and the peptides desalted on a reversed-phase SepPak C18 cartridge (Waters); peptides were eluted using 80% acetonitrile (ACN). The eluate was dried in a SpeedVac and the peptides acidified with 2% ACN-0.1% TFA.

Cellular proteome digestion

About 50 μg of proteins in 8 M guanidine were reduced with 10 mM dithiothreitol, alkylated with 30 mM iodoacetamide, sequentially digested with 1.0 μg LysC-tr and 1.0 μg trypsin as described above for secretome proteins.

Exosome digestion

The proteins present in the exosomes were separated from the lipid components by chloroform/methanol precipitation (27). After resuspension of the chloroform/methanol precipitation pellet in 45 μL of 8 M guanidine, proteins were reduced with DTT, alkylated with iodoacetamide, and sequentially digested with LysC-tr and trypsin as described above.

LC-MS/MS analysis

A nanoflow UHPLC instrument (Easy nLC, Thermo Fisher Scientific) was coupled on-line to a Q Exactive mass spectrometer (Thermo Fisher Scientific) with a nanoelectrospray ion source (Thermo Fisher Scientific). Peptides were loaded onto a C18 reversed-phase column (25 cm long, 75 μm inner diameter) and separated with a linear gradient of 5–35% buffer B (100% acetonitrile in 0.1% formic acid) at a flow rate of 300 nL/min over 240 min. MS data were acquired using a data-dependent Top15 method dynamically choosing the most abundant precursor ions from the survey scan (400–1400 m/z) using HCD fragmentation. Survey scans were acquired at a resolution of 70,000 at m/z 400. Unassigned precursor ion charge states as well as singly charged species were excluded from fragmentation. The isolation window was set to 3 Da and fragmented with a normalized collision energy of 27. The maximum ion injection times for the survey scan and the MS/MS scans were 20 ms and 60 ms, respectively, and the ion target values were set to 1e6 and 1e5, respectively. Selected sequenced ions were dynamically excluded for 30 seconds. Data were acquired using Xcalibur software (Thermo).

Data processing and bioinformatic analysis

Mass spectra were analyzed using MaxQuant software version 1.5.2.8 using the Andromeda search engine (28, 29). The initial maximum allowed mass deviation was set to 10 ppm for monoisotopic precursor ions and 0.5 Da for MS/MS peaks. Enzyme specificity was set to trypsin, defined as C-terminal to arginine and lysine excluding proline, and a maximum of two missed cleavages were allowed. Carbamidomethylcysteine was set as a fixed modification, and N-terminal acetylation and methionine oxidation as variable modifications. The spectra were searched with the Andromeda search engine against the Human and RSV SWISSPROT sequence database (containing 20,193 human protein entries and 11 RSV protein entries) combined with 248 common contaminants, and concatenated with the reversed versions of all sequences. Protein identification required at least one unique or razor peptide per protein group. Quantification in MaxQuant was performed using the built in XIC-based label-free quantification (LFQ) algorithm (29). The required false discovery rate (FDR) for identification was set to 1% at the peptide and 1% at the protein level, and the minimum required peptide length to 6 amino acids. Contaminants, reverse identification and proteins only identified by site were excluded from further data analysis. The raw data, and database search results are deposited in ProteomeXchange (http://

www.proteomexchange.org/) under Project Accession Number PXD005814. For comparative analysis, the LFQ values were log2-transfomed. After filtering (at least 2 valid LFQ values in at least one group), remaining missing LFQ values were imputed from a normal distribution (width: 0.3; down shift: 1.8). Significance analysis of microarrays (SAM) was used to assess the statistical significance of protein abundances using 1% FDR adjustment and a two-fold cutoff (30).

The normalized spectral abundance factor (NSAF) value for each protein was calculated as

$$(NSAF)_k=(I/L)_k/\sum_{i=1}^{N}(I/L)_i,$$

where the total MS intensity (I) of the matching peptides from protein k was divided by the protein length (L) and then by the sum of I/L for all uniquely identified proteins in the dataset (31).

For pairwise comparisons, missing NSAF values for proteins that were only present in either CM or the whole-cell lysate (WCL) were imputed from a normal distribution (width: 0.3; down shift: 1.8). For principal component analysis, unsupervised hierarchical clustering, GO annotation enrichment, and Fisher's exact tests, we used the Perseus bioinformatics platform (http://141.61.102.17/perseus_doku/doku.php?id=start). We used Ingenuity Pathways Analysis (IPA) for upstream regulator analysis. Gene set enrichment analysis was performed by quantifying canonical pathway enrichment (32). Exosome analyses were performed by searching the ExoCarta exosome database at http://www.exocarta.org/ (33).

Stable isotope dilution (SID)-selected reaction monitoring (SRM)-MS

The SID-SRM-MS assays were developed as described previously (34). The peptides were chemically synthesized incorporating isotopically labeled [$^{13}C_6{}^{15}N_4$] arginine or [$^{13}C_6{}^{15}N_2$] lysine to a 99% isotopic enrichment (Thermo Scientific). The secretome and cellular proteome were digested as described above. The tryptic digests were reconstituted in 30 μL of 5% formic acid/0.01% TFA. An aliquot of 10 μL of diluted stable isotope-labeled standard (SIS) peptides was added to each tryptic digest. These samples were desalted with a ZipTip C18 cartridge; the peptides were eluted with 80% can, dried, reconstituted in 30 μL of 5% formic acid/0.01% TFA, and directly analyzed by liquid chromatography (LC)-SRM-MS using a TSQ Vantage triple quadrupole mass spectrometer equipped with a nanospray source (Thermo Scientific, San Jose, CA). Online chromatography was performed using an Eksigent NanoLC-2D HPLC system (AB SCIEX, Dublin, CA). An aliquot of 10 μL of each tryptic digest was injected onto a C18 reversed-phase nano-HPLC column (PicoFrit™, 75 μm x 10 cm; tip ID 15 μm) at a flow rate of 500 nL/min with a 20-min 98% A, followed by a 15-min linear gradient from 2–30% mobile phase B (0.1 % formic acid/90% acetonitrile) in mobile phase A (0.1 % formic acid). The TSQ Vantage was operated in high-resolution SRM mode with Q1 and Q3 set to 0.2 and 0.7-Da Full Width Half Maximum (FWHM). All acquisition methods used the following parameters: 1800 V ion spray voltage, a 275°C ion transferring tube temperature, a collision-activated dissociation pressure at 1.5 mTorr, and the S-lens voltage used the values in the S-lens table generated during MS calibration.

All SRM data were manually inspected to ensure peak detection and accurate integration. The chromatographic retention time and the relative product ion intensities of the analyte peptides were compared to those of the SIS peptides. The variation of the retention time between the analyte peptides and their SIS counterparts should be within 0.05 min, and no significant differences in the relative product ion intensities of the analyte peptides and SIS peptides were observed. The peak areas in the extract ion chromatography of the native and SIS version of each signature peptide were integrated using Xcalibur® 2.1. The default values for noise percentage and baseline subtraction window were used. The ratios between the peak area of the native and SIS versions of each peptide were calculated.

Quantitative Real Time PCR (Q-RT-PCR)

For gene expression analyses, 1 μg of RNA was reverse-transcribed using Super Script III in a 20 μL reaction mixture (34). One μL of cDNA product was diluted 1:2, and 2 μL of diluted product was amplified in a 20 μL reaction mixture containing 10 μL of SYBR Green Supermix (Bio-Rad) and 0.4 μM each of forward and reverse gene-specific primers (Table I). The reaction mixtures were aliquoted into a Bio-Rad 96-well clear PCR plate and the plate sealed with Bio-Rad Microseal B film before insertion into the PCR machine. The plates were denatured for 90 s at 95°C and then subjected to 40 cycles of 15 s at 94°C, 60 s at 60°C, and 1 min at 72°C in an iCycler (Bio-Rad). PCR products were subjected to melting curve analysis to assure that a single amplification product was produced. Quantification of relative changes in gene expression was calculated using the ΔΔCt method (26). Data were expressed as fold change mRNA normalized to cyclophilin or PolB mRNA abundance as indicated as an internal control.

RSV infection in BALB/c mice

BALB/c mice (Harlan) were inoculated intranasally (in) with 50 μL of pRSV (final inoculum, 10^7 pfu) diluted in PBS under light anesthesia as previously described (35). Twenty-four hours later, the animals were euthanized and their lungs fixed in paraformaldehyde for immunohistochemical analysis. Sections were prepared and stained with H&E or Periodic Acid Schiff (Abcam) stains using standard techniques.

Results

Analysis pipeline for cell type-specific differences in the epithelial secretome

In the first experiment, we examined the effects of RSV on secreted proteins in hBECs derived from the trachea *vs* hSAECs, derived from the terminal bronchioles. Because tert-immortalized cells maintain a highly differentiated epithelial phenotype over continuous passages, we used these cells for establishing and validating a secretome analysis pipeline. Tert-hBECs form pseudostratified ciliated monolayers on air-liquid interfaces (22). By contrast, tert-hSAECs express high amounts of p63 aldehyde dehydrogenase, and differ from tert-hBECs by their resistance to naphthalene injury, a characteristic of bronchiolar cells (36).

Our previous work has shown that RSV effectively replicates in both cell types, expressing cytokines, producing infectious virions and syncytia formation (37, 38). To directly compare

the levels of RSV replication, tert-hBECs and tert-hSAECs were infected with sucrose cushion-purified (p)-RSV (MOI=1, 24 h). Cells were lysed and the expression of RSV nucleoprotein (N), matrix protein (M), phosphoprotein (P) and matrix M2-1 (M2-1) determined by LC-MS/MS (Fig. 1A). The levels of RSV expression for all proteins measured were dramatically elevated in tert-hBECs and tert-hSAECs relative to uninfected cells. Interestingly, RSV protein replication was 4-fold higher in tert-hBECs than in tert-hSAECs (Fig. 1A). Similar results were observed in the conditioned medium (CM) from each cell type (although the protein abundance was lower due to medium dilution), indicating viral secretion (Fig. 1B).

To determine the effects of RSV infection on cell viability, apoptosis and necrosis rates of control and RSV-infected tert-hBECs and tert-hSAECs (MOI=1, 24 h) were measured by flow cytometry. Cellular necrosis was minimal in both cell types in the absence or presence of RSV infection. However, in the absence of infection, tert-hBECs had a higher basal apoptotic rate than did tert-hSAECs (18.8% vs 10.8%, Fig. 1C). In both cell types, RSV infection reduced the apoptosis rate. The apoptotic rate of tert-hBECs fell from 18.8 to 12.5%, and of tert-hSAECs fell from 10.8% to 7.9% (Fig. 1C). These data are consistent with earlier studies demonstrating that cell death is not a major initial effect of RSV infection (39), and that the apoptosis rate is reduced upon RSV infection due to NFκB activation by the innate pathway, inducing anti-apoptotic genes (40). Together these data indicate that, under these conditions, the cells are viable, and actively replicating and secreting RSV.

We next sought to quantify the reproducibility of our label-free proteomics workflow to detect changes in secreted proteins by cell type and in response to RSV infection. Cell culture supernatants from 4 independent biological replicates from tert-hBECs vs tert-SAECs were analyzed in mock-infected cells and 24 h after RSV infection (Fig. 2A). 1,559 proteins were identified in the supernatants with a false discovery rate (FDR) of < 1%, determined by target-decoy database searching. To determine biological reproducibility, pairwise analysis of the log2-transformed protein abundance was performed. The Pearson correlations (r^2) were > 0.85, indicating a high degree of concordance (Table I, Supplemental Fig. S1). We noted that across samples, the r^2 was greater for the RSV-induced CM *vs* control (for control tert-hBECs, the groupwise mean $r^2 = 0.863 \pm 0.008$, whereas the RSV-infected tert-hBEC groupwise mean $r^2 = 0.957 \pm 0.005$; and for control tert-hSAECs, mean $r^2 = 0.863 \pm 0.01$ *vs* RSV-infected tert-hSAEC mean $r^2 = 0.936 \pm 0.011$; both $p<0.05$ Student's *t*-test). These data indicate that the method was reproducible, and that the highly abundant proteins in the RSV-induced CM were more accurately measured.

Secretome proteins are a distinct population of proteins from that produced by cellular lysis

To further extend our findings that the proteins in the secretome are not derived from cellular lysis, cellular lysates were prepared from the same experiment and analyzed in parallel (Fig 2A). 1,929 unique proteins were quantified from the tert-hBEC and tert-hSAEC whole-cell lysates (WCL). The global protein expression patterns in the CM and WCLs were first examined using principal component analysis (PCA). In this analysis, 91.6% of the

variability was accounted for in the first two dimensions, indicating a robust analysis (Fig. 2B). The WCLs from control or RSV-infected cells clustered by cell type and presence of RSV infection, indicating that biological replicates were consistent. We noted that the control tert-hBEC WCL formed a distinct cluster from that of the tert-hSAEC WCLs, separated by the second principal component dimension (Fig. 2B). The RSV-infected tert-hBEC WCLs moved in the second dimension to form a cluster that overlapped with both control and RSV-infected tert-hSAEC WCLs. Both the control secretomes of tert-hBECs and tert-hSAECs clustered together, widely separated in the first dimension from the WCL clusters. Upon RSV infection, both the tert-hBEC and tert-hSAEC secretomes migrated up in the second dimension and down in the first dimension (Fig. 2B). Together, these analyses indicate that the secretome represented a distinct protein set from the cellular lysate, and that RSV induced significant changes in its composition.

A Venn diagram comparison of the WCL vs the secretome is shown in Fig. 2C; 460 proteins were present only in the secretome, 885 proteins were unique to the cellular proteome, and 1,044 proteins were present in both datasets. To further confirm that these protein sets were distinct, we conducted unbiased genome ontology cellular component (GOCC) enrichment analysis of the proteins present only in the CM dataset. This analysis indicated that the secretome was enriched with proteins derived from the extracellular region part (205 out of 460 proteins), while the cytoplasmic and mitochondrial proteins were depleted (Fisher Exact test, Benjamini-Hochberg FDR 0.1%; data not shown). By contrast, proteins unique to the WCL were enriched with mitochondrial, ribosomal, and nuclear proteins, and proteins in the extracellular region were depleted.

To confirm that the secreted proteins were independent of cellular lysis in a more quantitative manner, we used the normalized spectral abundance factor (NSAF) method to confirm the enrichment of the proteins in CM and WCL. NSAF is a widely used spectral counting method for label-free proteomic quantitation (41–43). In spectral counting, larger proteins usually generate more peptides and therefore more spectral counts than smaller proteins. Therefore, the number of spectral counts for each protein is first divided by the protein length, which defines the spectral abundance factor (SAF). Furthermore, to accurately account for sample-to- sample variation, individual SAF values are normalized by dividing by the sum of all SAFs for proteins identified in the sample, resulting in the NSAF value (31). In this manner, NSAF values are standardized across distinct samples, allowing direct comparisons of the relative protein abundance across samples.

We then conducted a pairwise comparison of NSAF values of proteins in the RSV CM to that of the WCL in RSV-infected tert-hBECs (Fig. 2D). A two-sample *t*-test was used to assess the statistical significance of protein enrichment in the RSV CM to that of the WCL. For tert-hBECs, proteins enriched in the CM (indicated in red, Benjamini-Hochberg FDR 1%) included macrophage inhibitory factor (MIF-1), macrophage migration CXCL-10, interferon-stimulated gene-15, high mobility group box (HMGB) 1/2, interferon-induced protein with tetratricopeptide repeats (IFIT)-3, IFN lambda 2, and others. All of these proteins are well-characterized, secreted proteins with defined roles in innate immunity. The abundance of these proteins was depleted in the WCLs. Conversely, we identified high-abundance intracellular proteins in the cell extract (indicated in blue, Benjamini-Hochberg

FDR 1%) that were depleted in the CM, including histones H2HAC/1H2BM, mitochondrial single-stranded DNA-binding protein (SSBP)-1, heat shock 10kDa protein 1 (HSPE1), and actin gamma (ACTG)-1 (Fig. 2D).

Similar observations were made in the comparison of high-abundance proteins in the tert-hSAEC CM and WCLs (Fig. 2E). Although the proteins comprising the tert-hBEC and tert-hSAEC CM were similar, we noted that CCL5 was in high abundance in the tert-hBEC and much lower in the tert-hSAEC CM. Conversely, CCL20 and IL-6 were much more highly abundant in the tert-hSAEC secretome than in the tert-hBEC secretome (c.f. Figs. 2D, E). Together these data indicate that the CM samples represent a distinct proteome profile *vs* that in the WCL. We will refer to this population of proteins as the "secretome" in the remainder of this study.

Biological functions of the RSV-induced secretome

To further support the conclusion that the secretome and cell lysates represent distinct protein pools, we conducted unbiased genome ontology cellular component (GOCC) enrichment. The top-ranked cellular components for the RSV-induced secretome of tert-hBECs (indicated in red) were "extracellular matrix," "extracellular space" and "extracellular organelle," indicating that this sample was enriched in extracellular proteins relative to the reference human proteome (Fig. 2F). The cellular components corresponding to "cell part," "macromolecular complexes," and "ribonucleoprotein complexes" were depleted in the secretome (indicated in blue, Fig. 2F). By contrast, in the tert-hBEC WCLs, the GOCCs "nucleolar ribonucleoprotein complex," "NADH dehydrogenase complex," and "ribosomal complex" were the top-ranked components (red bars, Fig. 2F). Similarly, the "proteinaceous extracellular matrix" and "extracellular matrix" were the two most significantly depleted cellular components (blue bars, Fig. 2F). These data further support that the proteins identified in the secretome represent a distinct population from the intracellular proteome in the WCL. There were similar findings for tert-hSAECs, with extracellular proteins being the most highly enriched proteins in the hSAEC secretome GOCC analysis (Fig. 2G). We noted that the cellular component terms for the hBEC and hSAEC secretomes were almost identical (c.f. Figs 2F, G).

RSV induces exosome production in a cell type-dependent pattern

We noted that the majority of 1,044 proteins that were present in both the tert-hBEC and tert-hSAEC secretomes were cytosolic proteins. These cytosolic proteins may be secreted via unconventional protein secretory pathways, perhaps mediated by Golgi or endosomal export mechanisms (44). To this point, we found that 65 of these common proteins, including heat shock cognate 71 kDa protein (HSPA8), glyceraldehyde-3-phosphate GAPDH), and annexin A2 (ANXA2) (33) are prominent exosomal proteins. To provide some insight into whether endosomal transport was contributing to the RSV-induced secretome, we isolated and quantified exosomal proteins from control and RSV-infected tert-hBECs and tert-hSAECs.

Ultracentrifuge-purified exosomes manifested 112.8 ± 2.0 nm in size by dynamic light scattering, and exhibited a characteristic membrane composition in TEM (Fig. 3A). From

this fraction, 937 exosomal proteins were identified; of these, 564 proteins were identified in the secretome (Fig. 3B; the 373 proteins unique to the exosomal fraction were below the limit of detection and not observed in the secretome analysis). The 937 proteins were subjected to GOCC. Significantly enriched cellular components included lysosomal, vacuolar, and endoplasmic reticular (Fig. 3C). Out of 937 identified exosome proteins, 853 were quantified across the experimental groups. Pairwise comparison by cell type and presence of RSV infection was accomplished using Student's *t*-test, as shown in a Volcano plot, where the Log2 fold change is plotted vs the Log10-transformed p value (Fig. 3D). RSV infection caused up-regulation of 220 tert-hSAEC and 241 tert-hBEC exosomal proteins; and downregulation of 146 tert-hSAEC and 223 tert-hBEC exosomal proteins (FDR<0.05). The protein contents in the exosome also display cell type differences. In the basal state, 31 proteins were more abundant in the tert-hSAEC exosome fraction, while 60 proteins were more abundant in the tert-hBEC exosome fraction (FDR<0.05). After RSV infection, 273 exosome proteins were different by cell type, with 134 proteins more abundant in RSV-infected tert-hSAEC exosomes and 139 proteins more abundant in RSV-infected tert-hBEC exosomes (FDR<0.05).

We applied a statistical filter using a p value (Student's *t*-test with Benjamini-Hochberg FDR correction of <0.05) and an expression filter of ± 5-fold change between control vs RSV-infected NSAF to identify the most highly differentially expressed exosomal proteins. The expression patterns were next compared by hierarchical clustering (Fig. 3E). These data clearly indicate that the exosomal proteins are different by cell type, and modified by the presence of RSV infection.

Of the 559 proteins in the secretome not directly found in the exosomal fraction, 80 proteins have identifiable signal peptides, with the remainder being enriched in lysosomal and vacuolar proteins. These findings suggest that the RSV-induced epithelial secretome is mediated primarily by exosomal protein release, with a smaller fraction due to lysosome- or vacuole-mediated export, and a small fraction by classical protein secretion.

Differential expression patterns by cell type

We next examined the differential expression patterns of secretome by cell type. Statistical analysis of microarray (SAM) was applied to identify differentially expressed proteins using 1% false discovery rate (FDR). SAM identified 71 proteins distinct in the control secretomes from tert-hBECs *vs* tert-hSAECs (Fig. 4A). Of these, 61 were upregulated in the tert-hSAEC secretome. Similarly, 131 proteins showed differential expression in the RSV-induced secretomes from tert-hBECs and tert-hSAECS (Fig. 4B). Of these, 65 were upregulated in hSAECs.

The differentially expressed proteins were subjected to 2-dimensional hierarchical clustering. Hierarchical clustering groups proteins (rows) whose expression patterns are most similar across cell type and treatment condition. The samples (columns) are also clustered by the patterns of proteins. In this analysis, the treatment groups co-clustered in the vertical dimension, consistent with the findings in PCA analysis that the replicates from each cell type are highly similar (Fig. 4C). By inspection of the proteins in the rows, 5 distinct patterns of protein expression emerged. Cluster 1 represents proteins abundant in control

tert-hBECs whose expression is inhibited in response to RSV (not expressed by tert-hSAECs). Cluster 2 represents proteins expressed by tert-hSAECs whose abundance is decreased in response to RSV. Cluster 3 contains proteins only expressed by RSV-infected tert-hSAECs. Cluster 4 contains proteins induced by RSV that are common to both cell types. Cluster 5 contains proteins induced by tert-hBECs but not tert-hSAECs. We note that cluster 3 contains a number of immunologically significant proteins, including CXCL1, IL-6 and CCL20. These data suggest that RSV induces cell-type differences in the secretion of immunologically significant cytokines. Collectively, our analysis pipeline developed using tert-immortalized human epithelial cells, enables the reliable analysis of epithelial secretomes to understand differences by cell type and RSV-induced expression patterns.

Primary epithelial cell secretomes

We next applied our analysis pipeline to primary isolates of human BECs (phBECs) and primary isolates of SAECs (phSAECs). To control for donor effects, the analysis was conducted on three independent donors (donor demographic data are shown in Supplemental Table I); two biological replicates were analyzed for each. As validation of the distinct phenotypes, immunofluorescence microscopy was conducted to examine differences in epithelial cytokeratin expression. phBECs express cytokeratins 7 and 19; by contrast, hSAECs have low (or undetectable) cytokeratin 7 and strong cytokeratin 19 expression (Fig. 5A). Both cell types support active RSV replication and secretion of virus (not shown).

Secretome fractions were prepared from control and RSV-infected primary cells. We identified 2,376 proteins with FDR 1%. SAM analysis identified 577 proteins in the secretome from control (uninfected) cells whose expression varied by cell type, and 966 proteins in the secretome from RSV-infected cells whose expression varied by cell type (FDR of 1%). To focus on the most robust differentially expressed proteins, we filtered proteins that showed a 5-fold expression change or greater; this resulted in 492 of the most highly significant and induced proteins. This filtered dataset was subjected to 2-dimensional hierarchical clustering, where each column represents a sample and each row represents an individual protein's abundance. We observed that each sample co-clustered with its replicate, as well as by being grouped by cell type and RSV treatment (Fig. 5B). The row-wise clustering of proteins produced a pattern highly similar to that observed in the Tert-immortalized hBECs and hSAECs (c.f. Figs 5B and 4C); in this example, cluster 2 represents 11 proteins upregulated by RSV infection in phBECs; cluster 3 represents 116 proteins upregulated by RSV infection in phSAECs; and cluster 4 contains 203 proteins induced by both cell types (Table II).

Independent confirmation of differential secretion patterns

To validate the differentially expressed protein patterns, we independently quantified their expression using SID-SRM-MS. This method is a 'targeted' MS approach for the detection and accurate quantification of proteins in a complex background where signature proteotypic peptides unique to the protein of interest are monitored in a high mass accuracy mass spectrometer (34, 45–47). Because the peptide fragments are then subjected to fragmentation, the assay provides structural specificity and therefore is the most accurate approach available for direct quantification of target proteins in a complex mixture (47).

SRM assays were developed for the measurement of 15 proteins. These assays confirmed the constitutive cell type-specific expression of fibronectin (FN1), and the RSV-induced expression of guanine nucleotide-binding protein (GNAL2), annexin (ANA)-X2, ras oncogene (RAB)-7A, aldolase (ALDO)-A, heat shock protein (HSP)-90, vimentin (VIM), IL-6, integrin alpha 3 (ITGA3), caveolin (CAV)-1 and IFIT-1/2/3 by phSAECs (Fig. 6). These data indicated that RSV induces differential expression of proteins by cell type.

Biological Functions of Secreted Proteins

To gain further understanding of RSV-inducible proteins, we analyzed the clusters by GO biological function and Gene Set Enrichment Analysis (GSEA), primarily focusing on clusters 2, 3 and 4 (shown in Fig. 5B). The 11 proteins in cluster 2 were too limited to identify extensive enriched GO categories. Relative to the human proteome, cluster 2 was depleted in the GO category for metabolic process (Fig. 7A). GSEA showed enrichment for extrinsic prothrombin pathway and fibrinolysis pathway, predominantly determined by the presence of fibrinogen (Fig. 7A). The 116 proteins in cluster 3, uniquely expressed by RSV-infected hSAECs, showed enrichment for metabolic processes (organic acid, cellular ketone, and small molecule) relative to the human proteome, and depletion in RNA processing (Fig. 7B). GSEA identified enrichment of canonical pathways for glycoxylate, carbonyl, porphyrin and amino acid metabolism, and oxidative reduction (Fig. 7B). This analysis suggests that phSAECs secrete proteins controlling nucleotide-sugar bioenergetic processes in response to RSV.

The 203 proteins secreted by both epithelial cell types (cluster 4, Fig. 5B) were analyzed in the same manner. This analysis identified the most GO functions numerically, many of which could be collapsed into mRNA processing (splicing, catabolism, ribonuclease complex assembly), DNA cell cycle regulation and others (Fig. 7C). GSEA indicated enrichment in mRNA destabilization, Wnt signaling, HIV factor interactions and mRNA interaction/metabolism (Fig. 7C).

Upstream factor analysis of proteins unique to hSAECs

To obtain further insights into the differentially regulated proteins, we subjected all proteins showing differential expression to IPA upstream regulator analysis (48). Upstream regulator analysis compares the known effect (transcriptional activation or repression) of a transcriptional regulator on its target genes to the observed changes in protein abundance. In phBECs, the epithelium-specific ets homologous factor (EHF) was predicted to be more upregulated and responsible for regulating MUC1, serum amyloid A2 and kallikrein-related peptidase (KLK-6/7) (Fig. 8, left panel). In phSAECs, the NFκB transcription factor was predicted to be activated to a greater degree in response to RSV infection than in hBECs. The NFκB network is responsible for regulating TSLP, CCL20, BMP2, MMP3 and SOD2 (Fig. 8, right panel).

Secretion of Th2-differentiating and mucin-inducing cytokines

Our protein-level analysis of the proteins unique to hSAECs (cluster 3, Fig. 5B) identified three proteins highly relevant to the pathogenesis of RSV LRTI – TSLP, CCL20, and CCL3-L1. These proteins contain signal peptide sequences and are found in the free (non-exosomal

fraction). TSLP is produced by RSV-infected airway epithelium and promotes Th2 differentiation by inducing the maturation of antigen-presenting dendritic cells (49, 50). CCL20 is a potent inducer of epithelial mucin production (51), Th17 lymphocyte and dendritic cell chemotaxis that promotes formation of mucosal lymphoid tissue formation and plays an important role in the pathology of RSV-induced lung inflammation (52). Chemokine (C-C motif) ligand 3-like 1 (CCL3-L1) is chemotactic for monocytes and lymphocytes, and interacts with CCR5, a receptor linked to RSV LRTI (53).

We therefore selected these three immunologically important proteins previously implicated in the pathogenesis of RSV LRTI for validation experiments. To independently measure their differential expression by RSV infection and cell type, we developed and applied highly specific SID-SRM-MS assays to measure target protein abundance in the phBEC and phSAEC secretomes in the presence or absence of RSV infection. We were able to detect a 10-fold increase in CCL20, TSLP and CCL3-L1 expression in RSV-infected phSAECs relative to uninfected controls (Fig. 9A). By contrast, RSV-infected phBECs showed only 2-fold induction of each chemokine, and at much lower amounts than that in phSAECs (Fig. 9A). As shown in Fig. 9B, the presence or absence of the BSA/growth factor supplements in the cell culture medium did not affect the RSV-induced cell-type differences in the secretion of CCL20, TSLP and IL-6.

phSAEC-secreted CCL20 is a biologically active mucin inducer

Although mucins constitute an important arm of the innate immune response via their ability to trap microorganisms (54), mucins also play an important role in the pathogenesis of airway obstruction in RSV LRTI. As described earlier, mucous plugging of the small airways is an important mechanism for atelectasis in bronchiolitis, producing ventilation-perfusion mismatching and hypoxia (55, 56). To determine whether the RSV-induced CCL20 production was at levels sufficient for biological activity, we first evaluated whether phBECs express the CCR6 receptor CCR6 mRNA expression by Q-RT-PCR. Both cell types express CCR6 in uninfected and infected conditions (Fig. 9C). We next stimulated naïve phBECs with either recombinant CCL20 or CM from RSV-infected phSAECs and assayed for MUC5A mRNA expression by Q-RT-PCR. Recombinant CCL20 induced a reproducible 8-fold induction of MUC5AC mRNA expression relative to control, which was lost at higher concentrations (Fig. 9D). RSV-CM produced a similar 8-fold induction of MUC5A (Fig. 9E). Both of these activities were inhibited by the addition of neutralizing CCL20 Ab; pre-immune IgG had no effect (Fig. 9F, G). Together these data indicate that RSV-infected phSAECs produce biologically active CCL20 that stimulates mucin production.

Confirmation of enhanced CCL20 in lower airway epithelial cells in vivo

Our quantitative *in vitro* proteomic studies suggest that lower airway epithelial cells exhibit enhanced CCL20 secretion upon RSV infection. To confirm this, we examined CCL20 expression in a BALB/c mouse model of acute RSV infection established in our laboratories (57). Immunofluorescence (IF) assays were performed on proximal and distal airways in control and RSV-infected mice. In the absence of primary antibody, no fluorescence was observed (Fig. 10A). In proximal airways, IF was faintly distributed within the epithelial layer and weakly induced upon RSV infection (not shown). By contrast, CCL20 IF was

strongly induced in the smaller airways, both upon RSV infection (Fig. 10A). These (< 1mm diameter) airways were lined with single layer of cuboidal epithelium and lacked cartilage representing bronchiolar and terminal bronchiolar structures (adjacent to alveoli).

To examine whether enhanced mucin production was seen in this model, tissue sections were stained with PAS to assess mucin production. We observed enhanced PAS staining in these smaller, distal airways (Fig. 10B). Together, these studies confirm that lower airway epithelial cells in the distal airways produce enhanced CCL20 expression with increased mucin production in this mouse model of RSV infection.

Discussion

RSV is an important human pathogen representing the most common cause of childhood LRTI (7) and the leading cause of infant viral death (9). RSV directly replicating in the airway epithelium triggers pulmonary innate immune response. RSV replication produces the viral molecular patterns 5′-phosphorylated RNA and dsRNA that are recognized by the cytoplasmic RIG-I cytoplasmic pattern recognition receptor, which induces NFκB and IRF3 translocation and activation; these inducible transcription factors coordinate the expression of inflammatory chemokines via extensive cross-talk pathways (58). Consequently, infected epithelial cells rapidly secrete type I and -III IFNs (24, 37, 59), and 17 C-, CXC- and CC-type chemokines (15, 60, 61). How RSV infection of the lower airway contributes to the observed pathophysiology is largely unknown. Previous limited work comparing ciliated and transformed type II-like alveolar cells have found that these different cell types exhibit qualitatively distinct patterns of RSV-induced CC chemokine production (20). In this study, we apply unbiased proteomics to identify 577 high- confidence proteins whose RSV-induced expression patterns differ between primary human epithelial cells derived from the conductive airway (trachea) and those of the small airways (bronchioles). A surprising finding was that about third of the proteins identified in the secretome are exosomal. Although a number of RSV-inducible proteins are common, RSV induces a group of proteins unique to the phSAECs that are immunologically significant – TSLP, CCL20, CCL3-L1 and IL-6. Differential expression of these proteins was independently validated by specific SID-SRM-MS assays. We demonstrate that CCL20 is the major mucin-promoting cytokine in hSAECs secretome, and validate its preferential expression in lower airways in a BALB/c mouse model of RSV infection. These data advance our understanding of the epithelial innate response and provide insight into how RSV LRTI is associated with enhanced mucin production and lower airway obstruction.

The epithelial surface of the pulmonary mucosa consists of highly differentiated, regionally distinct epithelial cell types, each playing a specialized role in normal pulmonary function and host defense. Upper airway ciliated epithelial cells produce protective epithelial lining fluid and regulate water and ion transport, whereas pseudostratified tracheal airway cells produce mucins and coordinated ciliary beating to facilitate mucociliary particulate clearance (62). Despite a significant amount of cellular proteomic profiling of RSV-epithelial interactions (63–65), a systematic understanding of the spectrum of secreted proteins as a function of epithelial phenotype has not been obtained. In this study, we have selected a model of primary human airway epithelial cells cultured in submerged

monolayers. This cellular model has been extensively used for the study of innate responses to RSV and has provided important insights into the mechanisms of activation of the innate response and its subversion by RSV nonstructural proteins. Although growth under these conditions confer basal cell-like characteristics, recent studies have shown that basal cell infection is important for amplifying RSV infection in ciliated cells (66). Our validation of differential cytokine expression in the mouse model establishes further relevance of our findings to pulmonary host defense. An important extension of our work will be to conduct these studies in polarized cells in air-liquid interface.

Recent advances in secretome profiling have provided interesting insights into inducible protein secretion. Secretome profiling of macrophages using a proteomic pipeline similar to ours showed that TLR4 activation induced the production of over 775 proteins present in concentrations greater than 1 pg/ml (67). Like our study, the vast majority of secreted proteins that were identified included lysosomal, cytoplasmic and nuclear proteins – proteins that typically lack signal peptides. To minimize the possibility that these unconventionally secreted proteins represented cellular necrosis or apoptosis, we employed a lower MOI and sampled early time points, before significant apoptosis was produced in our experimental design. In fact, direct measurements of the apoptotic rate showed less apoptosis in RSV-infected than in control cells, due to the anti-apoptotic effects of NFκB demonstrated by earlier studies (40). Moreover, direct comparison of the secreted vs WCL proteomic profiles, functional classification by GO, and unbiased PCA clustering all consistently indicate that the CM and WCLs are drawn from distinct protein pools. Instead, we demonstrate here that a major fraction of secreted proteins from epithelial cells are contained within membrane-bound exosomes.

Exosomes are membrane-bound nanoparticles derived from intracellular multivesicular bodies that contain proteins and microRNAs important in intercellular communication (68). Studies on exosomes isolated from bronchoalveolar lavage samples of atopic asthmatics have shown that the exosomes may be involved in the regulation of bronchial hyperresponsiveness and inflammation (69, 70). Other studies have shown that exosomes isolated from highly differentiated ciliated tracheal epithelial cells mediate a protective antiviral response via the expression of sialoproteins that block influenza infection (71). Others have found that IL-13, a mediator of allergy and Th2 lymphocyte recruitment in asthma, induces exosome production in the airway that promotes the chemotaxis of macrophages (72). The role of exosomes in anti-RSV innate immunity and inflammation will require further exploration.

Additional proteins identified in the RSV secretome appear to be derived from unconventional protein secretory pathways. Our identification of lysosomal, vacuolar and nuclear proteins expressed in response to RSV replication suggests that unconventional protein secretion, perhaps through Golgi compartments, is also a component of the epithelial innate response.

Bioinformatic comparisons of the RSV-infected hBEC secretome *vs* the hSAEC secretome show that both cell types inducibly express over 200 common proteins. GO analysis indicate that these proteins play diverse functional roles. Although our focus is on proteins of

potential immunological importance to LRTIs, these data may help to identify other potential mechanisms of pulmonary innate defense. We note, for example, the presence of multiple types of RNA-binding proteins of distinct functional classes; these may serve to protect the airway by binding or metabolizing infectious nucleic acids. Similarly, the identification of Wnt signaling, an important epithelial morphogenic pathway (73), may provide clues to mechanisms of airway remodeling induced by RSV infection.

RSV LRTIs have been associated with Th2 polarization and enhanced aeroallergen sensitivity (74, 75). The epithelium plays an important role in shaping the T cell lymphocytic response through the patterns of chemokines and cytokines produced during infection. TSLP is an RSV-inducible, epithelium-derived chemokine important in allergic and RSV-induced airway inflammation (76, 77) secreted by airway cells in an NFκB-dependent mechanism (49) consistent with our upstream factor analysis. Although TSLP has a broad variety of target cell responses, its ability to activate pDC populations and promote Th2 lymphocyte-predominant inflammation is especially relevant to the pathophysiology of severe LRTI infection. Similarly, CCL20 is important in pDC activation and the recruitment of Th17 lymphocytes to sites of inflammation (78). The actions of Th17 cells have been also implicated in the pathogenesis of RSV LRTI (79), where clinical studies in children with severe RSV infection showed increased IL-17 levels in their airway fluids. Interestingly IL-17 appeared to be proinflammatory and pro-mucinogenic, yet paradoxically is protective against hypoxia (79). Our study surprisingly shows the novel observation that TSLP and CCL20 are preferentially secreted by RSV-infected lower airway epithelial cells, perhaps providing information on how LRTI is associated with Th2 lymphocyte skewing, DC recruitment and Th17 activation.

Severe RSV infections produce a characteristic pathological pattern that includes epithelial necrosis, sloughing and mucous plugging of the small bronchioles, resulting clinically in hypoxia and hyper-aeration (12, 55, 56). Mucous plugging is a complex phenomenon determined by both viral and host factors. Although the RSV nonstructural protein NS2 has been demonstrated to induce shedding of bronchiolar epithelial cells (12), the mechanisms for enhanced mucin production in RSV infection are not well understood. Rodent models of RSV disease have not consistently shown high levels of mucin production, unless the animals have had prior allergic sensitization (80), or strains of RSV are used that selectively induce IL-13 production (81).

In this study, we observe that RSV-induced CCL20 production is restricted to the epithelium, and that it preferentially secreted by lower airway cells. Other elegant studies have shown that CCL20 plays a pathogenic role in the mouse model of infection. Here knockouts of the CCL20 receptor (CCR6) or CCL20 neutralization have shown that inhibition of the CCL20-CCR6 axis decreases RSV-induced MUC5a and Gob5 expression and Th2 responses (52). Our have demonstrated that CCL20 is the major biological protein inducing mucin production secreted from RSV-infected hSAECs. Interestingly, the molecular pathway producing MUC5A expression is mediated by cleavage of the EGFR ligand by the cell-surface ADAM17/TACE distintegrin (51). This previous study was unable to induce MUC production in primary airway epithelial cells; here we demonstrate both recombinant CCL20 and CCL20 in hSAEC CM induces MUC5A expression in phBECs, and that phBECs

express CCR6R. The explanation for these different results may be due to cell-type differences in expression of the ADAM17/TACE distintegrin, or variability in CCR6 expression in cultured cells.

In summary, we apply quantitative, label-free mass spectrometry profiling to identify cell type-specific patterns in RSV-induced protein secretion that arises from the exosomal compartment. We validate the differential secretion patterns across multiple donors, and confirm our findings in a mouse model *in vivo*. We demonstrate that lower airway secretion of CCL20 is a mucin-promoting factor that may account for enhanced mucous plugging in distal airways in RSV LRTIs. These data provide insights into the pathogenesis of Th2 polarization and mucus plugging in this disease.

Supplementary Material

Refer to Web version on PubMed Central for supplementary material.

Acknowledgments

Research support was provided by the Sealy Center for Molecular Medicine, NIAID Signaling in Airway inflammation P01 AI068865 (ARB), UTMB CTSA UL1TR001439 (ARB), NIEHS P30 ES006676 (ARB), and NSF DMS-1361411/DMS-1361318 (ARB).

Core laboratory support was provided by the Sealy Center for Molecular Medicine Selected Reaction Monitoring facility and the UTMB Optical imaging and Histochemistry Facilities. We thank Dr. David Konkel for critically editing the manuscript.

Abbreviations used in this article

CCL20	Chemokine (C-C Motif) Ligand 20
CCL3-L1	chemokine (CC) ligand 3-like 1
EHF	epithelial-specific ets homology factor
FDR	false discovery rate
GO	gene ontology
GOCC	GO Cellular Component enrichment
GSEA	gene set enrichment analysis
hBEC	human bronchial epithelial cell
hSAEC	human small airway epithelial cell
LC-MS/MS	liquid chromatography - tandem mass spectrometry
NSAF	normalized spectral abundance factor
PCA	principal component analysis
RSV	respiratory syncytial virus

SID	stable isotopic dilution
SAM	statistical analysis of microarray
SRM	selected reaction monitoring
Tert	human telomerase
TSLP	thymic stromal lymphopoietin
WCL	whole cell lysate

References

1. Hall CB, Weinberg GA, Iwane MK, Blumkin AK, Edwards KM, Staat MA, Auinger P, Griffin MR, Poehling KA, Erdman D, et al. The Burden of Respiratory Syncytial Virus Infection in Young Children. The New England Journal of Medicine. 2009; 360(6):588–98. [PubMed: 19196675]
2. Easton AJ, Domachowske JB, Rosenberg HF. Animal Pneumoviruses: Molecular Genetics and Pathogenesis. Clinical Microbiology Reviews. 2004; 17(2):390–412. [PubMed: 15084507]
3. Hall CB, Weinberg GA, Blumkin AK, Edwards KM, Staat MA, Schultz AF, Poehling KA, Szilagyi PG, Griffin MR, Williams JV, et al. Respiratory syncytial virus-associated hospitalizations among children less than 24 months of age. Pediatrics. 2013; 132(2):e341–8. [PubMed: 23878043]
4. Collins PL, Graham BS. Viral and host factors in human respiratory syncytial virus pathogenesis. J Virol. 2008; 82(5):2040–55. [PubMed: 17928346]
5. Zorc JJ, Hall CB. Bronchiolitis: Recent Evidence on Diagnosis and Management. Pediatrics (Evanston IL). 2010; 125(2):342–9.
6. Moore ML, Stokes KL, Hartert TV. The impact of viral genotype on pathogenesis and disease severity: respiratory syncytial virus and human rhinoviruses. Curr Opin Immunol. 2013; 25(6):761–8. [PubMed: 24455766]
7. Hall CB. Respiratory syncytial virus and parainfluenza virus. New England Journal of Medicine. 2001; 344:1917–28. [PubMed: 11419430]
8. Shay DK, Holman RC, Newman RD, Liu LL, Stout JW, Anderson LJ. Bronchiolitis-associated hospitalizations among US children, 1980–1996. Journal of the American Medical Association. 1999; 282:1440–6. [PubMed: 10535434]
9. Nair H, Nokes DJ, Gessner BD, Dherani M, Madhi SA, Singleton RJ, O'Brien KL, Roca A, Wright PF, Bruce N, et al. Global burden of acute lower respiratory infections due to respiratory syncytial virus in young children: a systematic review and meta-analysis. Lancet. 2010; 375(9725):1545–55. [PubMed: 20399493]
10. Sigurs N, Gustafsson PM, Bjarnason R, Lundberg F, Schmidt S, Sigurbergsson F, Kjellman B. Severe respiratory syncytial virus bronchiolitis in infancy and asthma and allergy at age 13. Am J Respir Crit Care Med. 2005; 171(2):137–41. [PubMed: 15516534]
11. Richardson LS, Belshe RB, Sly DL, London WT, Prevar DA, Camargo E, Chanock RM. Experimental respiratory syncytial virus pneumonia in cebus monkeys. Journal of Medical Virology. 1978; 2(1):45–59. [PubMed: 210254]
12. Liesman RM, Buchholz UJ, Luongo CL, Yang L, Proia AD, DeVincenzo JP, Collins PL, Pickles RJ. RSV-encoded NS2 promotes epithelial cell shedding and distal airway obstruction. The Journal of Clinical Investigation. 2014; 124(5):2219–33. [PubMed: 24713657]
13. Garofalo RP, Haeberle H. Epithelial regulation of innate immunity to respiratory syncytial virus. American Journal of Respiratory Cell and Molecular Biology. 2000; 23:581–5. [PubMed: 11062135]
14. Tian B, Zhang Y, Luxon BA, Garofalo RP, Casola A, Sinha M, Brasier AR. Identification of NF-kappaB-dependent gene networks in respiratory syncytial virus-infected cells. J Virol. 2002; 76(13):6800–14. [PubMed: 12050393]

15. Zhang Y, Luxon BA, Casola A, Garofalo RP, Jamaluddin M, Brasier AR. Expression of respiratory syncytial virus-induced chemokine gene networks in lower airway epithelial cells revealed by cDNA microarrays. J Virol. 2001; 75(19):9044–58. [PubMed: 11533168]
16. Bennett BL, Garofalo RP, Cron SG, Hosakote YM, Atmar RL, Macias CG, Piedra PA. Immunopathogenesis of respiratory syncytial virus bronchiolitis. J Infect Dis. 2007; 195(10): 1532–40. [PubMed: 17436234]
17. Holt PG, Strickland DH, Wikstrom ME, Jahnsen FL. Regulation of immunological homeostasis in the respiratory tract. Nature reviews Immunology. 2008; 8(2):142–52.
18. Choudhary S, Boldogh I, Brasier AR. Inside-out signaling pathways from nuclear reactive oxygen species control pulmonary innate immunity. Journal of innate immunity. 2016
19. Whitsett JA, Alenghat T. Respiratory epithelial cells orchestrate pulmonary innate immunity. Nat Immunol. 2015; 16(1):27–35. [PubMed: 25521682]
20. Olzewska B, Casola A, Saito T, Alam R, Crowe S, Mei F, Ogra PL, Garofalo R. Cell-specific expression of RANTES, MCP-1, and MIP-1a by lower airway epithelial cells and eosinophils infected with respiratory syncytial virus. Journal of Virology. 1998; 72:4756–64. [PubMed: 9573240]
21. Welliver TP, Garofalo RP, Hosakote Y, Hintz KH, Avendano L, Sanchez K, Velozo L, Jafri H, Chavez-Bueno S, Ogra PL, et al. Severe Human Lower Respiratory Tract Illness Caused by Respiratory Syncytial Virus and Influenza Virus Is Characterized by the Absence of Pulmonary Cytotoxic Lymphocyte Responses. The Journal of Infectious Diseases. 2007; 195(8):1126–36. [PubMed: 17357048]
22. Ramirez RD, Sheridan S, Girard L, Sato M, Kim Y, Pollack J, Peyton M, Zou Y, Kurie JM, Dimaio JM, et al. Immortalization of human bronchial epithelial cells in the absence of viral oncoproteins. Cancer Res. 2004; 64(24):9027–34. [PubMed: 15604268]
23. Kalita M, Tian B, Gao B, Choudhary S, Wood TG, Carmical JR, Boldogh I, Mitra S, Minna JD, Brasier AR. Systems Approaches to Modeling Chronic Mucosal Inflammation. BioMed Research International. 2013:505864. [PubMed: 24228254]
24. Garofalo R, Mei F, Manganaro M, Espejo R, Ogra PL, Reyes VE. Upregulation of class I major histocompatibility complex (MHC) molecules on respiratory syncytial virus (RSV)-infected airway epithelial cells. American Journal of Respiratory and Critical Care Medicine. 1994; 149:A987.
25. Kalita MK, Sargsyan K, Tian B, Paulucci-Holthauzen A, Najm HN, Debusschere BJ, Brasier AR. Sources of cell-to-cell variability in canonical nuclear factor-kappaB (NF-kappaB) signaling pathway inferred from single cell dynamic images. J Biol Chem. 2011; 286(43):37741–57. [PubMed: 21868381]
26. Brasier AR, Tian B, Jamaluddin M, Kalita MK, Garofalo RP, Lu M. RelA Ser276 phosphorylation-coupled Lys310 acetylation controls transcriptional elongation of inflammatory cytokines in respiratory syncytial virus infection. J Virol. 2011; 85(22):11752–69. [PubMed: 21900162]
27. Wessel D, Flugge UI. A method for the quantitative recovery of protein in dilute solution in the presence of detergents and lipids. Anal Biochem. 1984; 138(1):141–3. [PubMed: 6731838]
28. Cox J, Mann M. MaxQuant enables high peptide identification rates, individualized p.p.b.-range mass accuracies and proteome-wide protein quantification. Nat Biotechnol. 2008; 26(12):1367–72. [PubMed: 19029910]
29. Cox J, Hein MY, Luber CA, Paron I, Nagaraj N, Mann M. Accurate proteome-wide label-free quantification by delayed normalization and maximal peptide ratio extraction, termed MaxLFQ. Molecular & cellular proteomics : MCP. 2014; 13(9):2513–26. [PubMed: 24942700]
30. Tusher VG, Tibshirani R, Chu G. Significance analysis of microarrays applied to the ionizing radiation response. Proc Natl Acad Sci U S A. 2001; 98(9):5116–21. [PubMed: 11309499]
31. Zybailov B, Mosley AL, Sardiu ME, Coleman MK, Florens L, Washburn MP. Statistical analysis of membrane proteome expression changes in Saccharomyces cerevisiae. J Proteome Res. 2006; 5(9):2339–47. [PubMed: 16944946]
32. Subramanian A, Tamayo P, Mootha VK, Mukherjee S, Ebert BL, Gillette MA, Paulovich A, Pomeroy SL, Golub TR, Lander ES, et al. Gene set enrichment analysis: a knowledge-based

approach for interpreting genome-wide expression profiles. Proc Natl Acad Sci USA. 2005; 102(43):15545–50. [PubMed: 16199517]

33. Keerthikumar S, Chisanga D, Ariyaratne D, Al Saffar H, Anand S, Zhao K, Samuel M, Pathan M, Jois M, Chilamkurti N, et al. ExoCarta: A Web-Based Compendium of Exosomal Cargo. J Mol Biol. 2016; 428(4):688–92. [PubMed: 26434508]
34. Zhao Y, Brasier AR. Applications Of Selected Reaction Monitoring (SRM)-Mass Spectrometry (MS) For Quantitative Measurement Of Signaling Pathways. Methods. 2013
35. Haeberle HA, Takizawa R, Casola A, Brasier AR, Dieterich HJ, Van Rooijen N, Gatalica Z, Garofalo RP. Respiratory syncytial virus-induced activation of nuclear factor-kappaB in the lung involves alveolar macrophages and toll-like receptor 4-dependent pathways. J Infect Dis. 2002; 186(9):1199–206. [PubMed: 12402188]
36. Gao B, Huang C, Sullivan JP, Spinola M, Gabriela Raso M, Wistuba I, Shay J, Minna JD. Immortalization of human small airway epithelial cells with characteristics of bronchioalveolar stem cells. FASEB J. 2009; 23 Meeting Abstract.
37. Tian B, Zhao Y, Kalita M, Edeh CB, Paessler S, Casola A, Teng MN, Garofalo RP, Brasier AR. CDK9-dependent transcriptional elongation in the innate interferon-stimulated gene response to respiratory syncytial virus infection in airway epithelial cells. J Virol. 2013; 87(12):7075–92. [PubMed: 23596302]
38. Fang L, Choudhary S, Tian B, Boldogh I, Yang C, Ivanciuc T, Ma Y, Garofalo RP, Brasier AR. Ataxia Telangiectasia Mutated Kinase Mediates NF-kappaB Serine 276 Phosphorylation and Interferon Expression via the IRF7-RIG-I Amplification Loop in Paramyxovirus Infection. J Virol. 2015; 89(5):2628–42. [PubMed: 25520509]
39. Zhang L, Peeples ME, Boucher RC, Collins PL, Pickles RJ. Respiratory Syncytial Virus Infection of Human Airway Epithelial Cells Is Polarized, Specific to Ciliated Cells, and without Obvious Cytopathology. The Journal of Virology. 2002; 76(11):5654–66. [PubMed: 11991994]
40. Thomas KW, Monick MM, Staber JM, Yarovinsky T, Carter AB, Hunninghake GW. Respiratory Syncytial Virus Inhibits Apoptosis and Induces NF-kappa B Activity through a Phosphatidylinositol 3-Kinase-dependent Pathway. Journal of Biological Chemistry. 2002; 277(1): 492–501. [PubMed: 11687577]
41. Liu H, Sadygov RG, Yates JR III. A model for random sampling and estimation of relative protein abundance in shotgun proteomics. Anal Chem. 2004; 76(14):4193–201. [PubMed: 15253663]
42. Old WM, Meyer-Arendt K, Aveline-Wolf L, Pierce KG, Mendoza A, Sevinsky JR, Resing KA, Ahn NG. Comparison of label-free methods for quantifying human proteins by shotgun proteomics. Molecular & cellular proteomics : MCP. 2005; 4(10):1487–502. [PubMed: 15979981]
43. Paoletti AC, Parmely TJ, Tomomori-Sato C, Sato S, Zhu D, Conaway RC, Conaway JW, Florens L, Washburn MP. Quantitative proteomic analysis of distinct mammalian Mediator complexes using normalized spectral abundance factors. Proc Natl Acad Sci U S A. 2006; 103(50):18928–33. [PubMed: 17138671]
44. Nickel W, Rabouille C. Mechanisms of regulated unconventional protein secretion. Nat Rev Mol Cell Biol. 2009; 10(2):148–55. [PubMed: 19122676]
45. Zhao Y, Tian B, Edeh CB, Brasier AR. Quantitation of the dynamic profiles of the innate immune response using multiplex selected reaction monitoring-mass spectrometry. Molecular & cellular proteomics : MCP. 2013; 12:1513–29. [PubMed: 23418394]
46. Zhao YX, Widen SG, Jamaluddin M, Tian B, Wood TG, Edeh CB, Brasier AR. Quantification of Activated NF-kappa B/RelA Complexes Using ssDNA Aptamer Affinity - Stable Isotope Dilution-Selected Reaction Monitoring-Mass Spectrometry. Molecular & Cellular Proteomics. 2011; 10(6)
47. Gerber SA, Rush J, Stemman O, Kirschner MW, Gygi SP. Absolute quantification of proteins and phosphoproteins from cell lysates by tandem MS. Proceedings of the National Academy of Sciences. 2003; 100(12):6940–5.
48. Kramer A, Green J, Pollard J Jr, Tugendreich S. Causal analysis approaches in Ingenuity Pathway Analysis. Bioinformatics. 2014; 30(4):523–30. [PubMed: 24336805]
49. Lee HC, Headley MB, Loo YM, Berlin A, Gale M Jr, Debley JS, Lukacs NW, Ziegler SF. Thymic stromal lymphopoietin is induced by respiratory syncytial virus-infected airway epithelial cells and

promotes a type 2 response to infection. The Journal of allergy and clinical immunology. 2012; 130(5):1187–96. e5. [PubMed: 22981788]

50. Reche PA, Soumelis V, Gorman DM, Clifford T, Liu M-r, Travis M, Zurawski SM, Johnston J, Liu Y-J, Spits H, et al. Human Thymic Stromal Lymphopoietin Preferentially Stimulates Myeloid Cells. The Journal of Immunology. 2001; 167(1):336–43. [PubMed: 11418668]
51. Kim S, Lewis C, Nadel JA. CCL20/CCR6 feedback exaggerates epidermal growth factor receptor-dependent MUC5AC mucin production in human airway epithelial (NCI-H292) cells. Journal of immunology (Baltimore, Md : 1950). 2011; 186(6):3392–400.
52. Kallal LE, Schaller MA, Lindell DM, Lira SA, Lukacs NW. CCL20/CCR6 blockade enhances immunity to RSV by impairing recruitment of DC. Eur J Immunol. 2010; 40(4):1042–52. [PubMed: 20101616]
53. Hull J, Rowlands K, Lockhart E, Moore C, Sharland M, Kwiatkowski D. Variants of the Chemokine Receptor CCR5 Are Associated with Severe Bronchiolitis Caused by Respiratory Syncytial Virus. Journal of Infectious Diseases. 2003; 188(6):904–7. [PubMed: 12964123]
54. Roy MG, Livraghi-Butrico A, Fletcher AA, McElwee MM, Evans SE, Boerner RM, Alexander SN, Bellinghausen LK, Song AS, Petrova YM, et al. Muc5b is required for airway defence. Nature. 2014; 505(7483):412–6. [PubMed: 24317696]
55. Aherne WT, Bird T, Court SDB, Gardner PS, McQuillin J. Pathological changes in virus infections of the lower respiratory tract in children. Journal Clinical Pathology. 1970; 23:7–18.
56. Ferris JA, Aherne WA, Locke WS. Sudden and unexpected deaths to infants: histology and virology. British Medical Journal. 1973; 2:439–49. [PubMed: 4351352]
57. Haeberle HA, Casola A, Gatalica Z, Petronella S, Dieterich HJ, Ernst PB, Brasier AR, Garofalo RP. IkappaB kinase is a critical regulator of chemokine expression and lung inflammation in respiratory syncytial virus infection. J Virol. 2004; 78(5):2232–41. [PubMed: 14963119]
58. Bertolusso R, Tian B, Zhao Y, Vergara LA, Sabree A, Iwanaszko M, Lipniacki T, Brasier A, Kimmel M. Dynamic Cross Talk Model Of The Epithelial Innate Immune Response To Double-Stranded Rna Stimulation: Coordinated Dynamics Emerging From Cell-Level Noise. PLoS ONE. 2014; 9(4):e93396. [PubMed: 24710104]
59. Jamaluddin M, Wang S, Garofalo RP, Elliott T, Casola A, Baron S, Brasier AR. IFN-beta mediates coordinate expression of antigen-processing genes in RSV-infected pulmonary epithelial cells. American journal of physiology Lung cellular and molecular physiology. 2001; 280(2):L248–57. [PubMed: 11159003]
60. Bao X, Liu T, Shan Y, Li K, Garofalo RP, Casola A. Human metapneumovirus glycoprotein G inhibits innate immune responses. PLoS Pathog. 2008; 4(5):e1000077. [PubMed: 18516301]
61. Bao X, Liu T, Spetch L, Kolli D, Garofalo RP, Casola A. Airway epithelial cell response to human metapneumovirus infection. Virology (New York NY). 2007; 368(1):91–101.
62. Knight DA, Holgate ST. The airway epithelium: structural and functional properties in health and disease. Respirology. 2003; 8(4):432–46. [PubMed: 14708552]
63. Brasier AR, Spratt H, Wu Z, Boldogh I, Zhang Y, Garofalo RP, Casola A, Pashmi J, Haag A, Luxon B, et al. Nuclear heat shock response and novel nuclear domain 10 reorganization in respiratory syncytial virus-infected a549 cells identified by high-resolution two-dimensional gel electrophoresis. J Virol. 2004; 78(21):11461–76. [PubMed: 15479789]
64. Munday DC, Emmott E, Surtees R, Lardeau CH, Wu W, Duprex WP, Dove BK, Barr JN, Hiscox JA. Quantitative proteomic analysis of A549 cells infected with human respiratory syncytial virus. Molecular & cellular proteomics : MCP. 2010; 9(11):2438–59. [PubMed: 20647383]
65. Ternette N, Wright C, Kramer HB, Altun M, Kessler BM. Label-free quantitative proteomics reveals regulation of interferon-induced protein with tetratricopeptide repeats 3 (IFIT3) and 5′-3′-exoribonuclease 2 (XRN2) during respiratory syncytial virus infection. Virology journal. 2011; 8(1):1–13. [PubMed: 21205327]
66. Persson BD, Jaffe AB, Fearns R, Danahay H. Respiratory syncytial virus can infect basal cells and alter human airway epithelial differentiation. PLoS One. 2014; 9(7):e102368. [PubMed: 25033192]
67. Meissner F, Scheltema RA, Mollenkopf H-J, Mann M. Direct Proteomic Quantification of the Secretome of Activated Immune Cells. Science. 2013; 340(6131):475–8. [PubMed: 23620052]

68. Thery C, Zitvogel L, Amigorena S. Exosomes: composition, biogenesis and function. Nature reviews Immunology. 2002; 2(8):569–79.
69. Levanen B, Bhakta NR, Torregrosa Paredes P, Barbeau R, Hiltbrunner S, Pollack JL, Skold CM, Svartengren M, Grunewald J, Gabrielsson S, et al. Altered microRNA profiles in bronchoalveolar lavage fluid exosomes in asthmatic patients. The Journal of allergy and clinical immunology. 2013; 131(3):894–903. [PubMed: 23333113]
70. Torregrosa Paredes P, Esser J, Admyre C, Nord M, Rahman QK, Lukic A, Radmark O, Gronneberg R, Grunewald J, Eklund A, et al. Bronchoalveolar lavage fluid exosomes contribute to cytokine and leukotriene production in allergic asthma. Allergy. 2012; 67(7):911–9. [PubMed: 22620679]
71. Kesimer M, Scull M, Brighton B, DeMaria G, Burns K, O'Neal W, Pickles RJ, Sheehan JK. Characterization of exosome-like vesicles released from human tracheobronchial ciliated epithelium: a possible role in innate defense. The FASEB Journal. 2009; 23(6):1858–68. [PubMed: 19190083]
72. Kulshreshtha A, Ahmad T, Agrawal A, Ghosh B. Proinflammatory role of epithelial cell-derived exosomes in allergic airway inflammation. The Journal of allergy and clinical immunology. 2013; 131(4):1194–203. 203.e1–14. [PubMed: 23414598]
73. Komiya Y, Habas R. Wnt signal transduction pathways. Organogenesis. 2008; 4(2):68–75. [PubMed: 19279717]
74. Sigurs N, Aljassim F, Kjellman B, Robinson PD, Sigurbergsson F, Bjarnason R, Gustafsson PM. Asthma and allergy patterns over 18 years after severe RSV bronchiolitis in the first year of life. Thorax. 2010; 65(12):1045–52. [PubMed: 20581410]
75. Sigurs N, Bjarnason R, Sigurbergsson F. Eosinophil cationic protein in nasal secretion and in serum and myeloperoxidase in serum in respiratory syncytial virus bronchiolitis: relation to asthma and atopy. Acta Pediatr. 1994; 83:1151–5.
76. Allakhverdi Z, Comeau MR, Jessup HK, Yoon BR, Brewer A, Chartier S, Paquette N, Ziegler SF, Sarfati M, Delespesse G. Thymic stromal lymphopoietin is released by human epithelial cells in response to microbes, trauma, or inflammation and potently activates mast cells. J Exp Med. 2007; 204(2):253–8. [PubMed: 17242164]
77. Ziegler SF, Roan F, Bell BD, Stoklasek TA, Kitajima M, Han H. The biology of thymic stromal lymphopoietin (TSLP). Adv Pharmacol. 2013; 66:129–55. [PubMed: 23433457]
78. Yamazaki T, Yang XO, Chung Y, Fukunaga A, Nurieva R, Pappu B, Martin-Orozco N, Kang HS, Ma L, Panopoulos AD, et al. CCR6 regulates the migration of inflammatory and regulatory T cells. Journal of immunology (Baltimore, Md : 1950). 2008; 181(12):8391–401.
79. Mangodt TC, Van Herck MA, Nullens S, Ramet J, De Dooy JJ, Jorens PG, De Winter BY. The role of Th17 and Treg responses in the pathogenesis of RSV infection. Pediatr Res. 2015; 78(5):483–91. [PubMed: 26267154]
80. Hashimoto K, Graham BS, Ho SB, Adler KB, Collins RD, Olson SJ, Zhou W, Suzutani T, Jones PW, Goleniewska K, et al. Respiratory syncytial virus in allergic lung inflammation increases Muc5ac and gob-5. Am J Respir Crit Care Med. 2004; 170(3):306–12. [PubMed: 15130904]
81. Moore ML, Chi MH, Luongo C, Lukacs NW, Polosukhin VV, Huckabee MM, Newcomb DC, Buchholz UJ, Crowe JE Jr, Goleniewska K, et al. A chimeric A2 strain of respiratory syncytial virus (RSV) with the fusion protein of RSV strain line 19 exhibits enhanced viral load, mucus, and airway dysfunction. J Virol. 2009; 83(9):4185–94. [PubMed: 19211758]

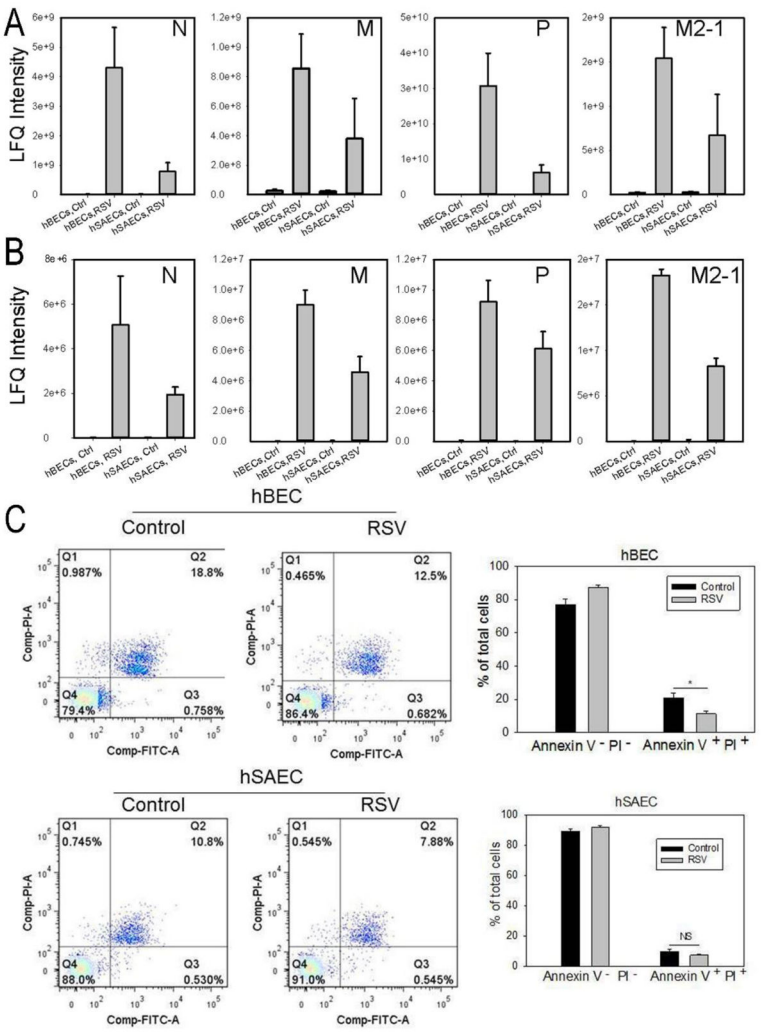

FIGURE 1. RSV replication and its effects on tert-immortalized epithelial cells

(A). Tert-hBECs or tert-hSAECs were infected with sucrose cushion-purified pRSV (MOI=1.0). 24 h later, cells were lysed and a panel of RSV nucleoprotein (N), matrix protein (M), phosphoprotein (P) and matrix M2-1 (M2-1) was quantified by LC-MS/MS. RSV proteins were not detected in mock-infected cells, and dramatically increased with infection. Note that RSV replicates more effectively in tert-hBECs. **(B).** CM was analyzed for RSV proteins as in Fig. 1A. (**C).** Fluorescence-activated cell sorting (FACS) showing percentage of apoptotic (lower right quadrant –annexin V-positive, PI-negative) and necrotic (upper right quadrant – annexin V-, PI-positive) cells after 24h of RSV infection. Bottom left, histogram of percentage of apoptotic tert-hBECs infected with RSV. Bottom right, histogram of percentage of apoptotic tert-hSAECs after RSV infection. Results are means ± SD of duplicates measured twice.

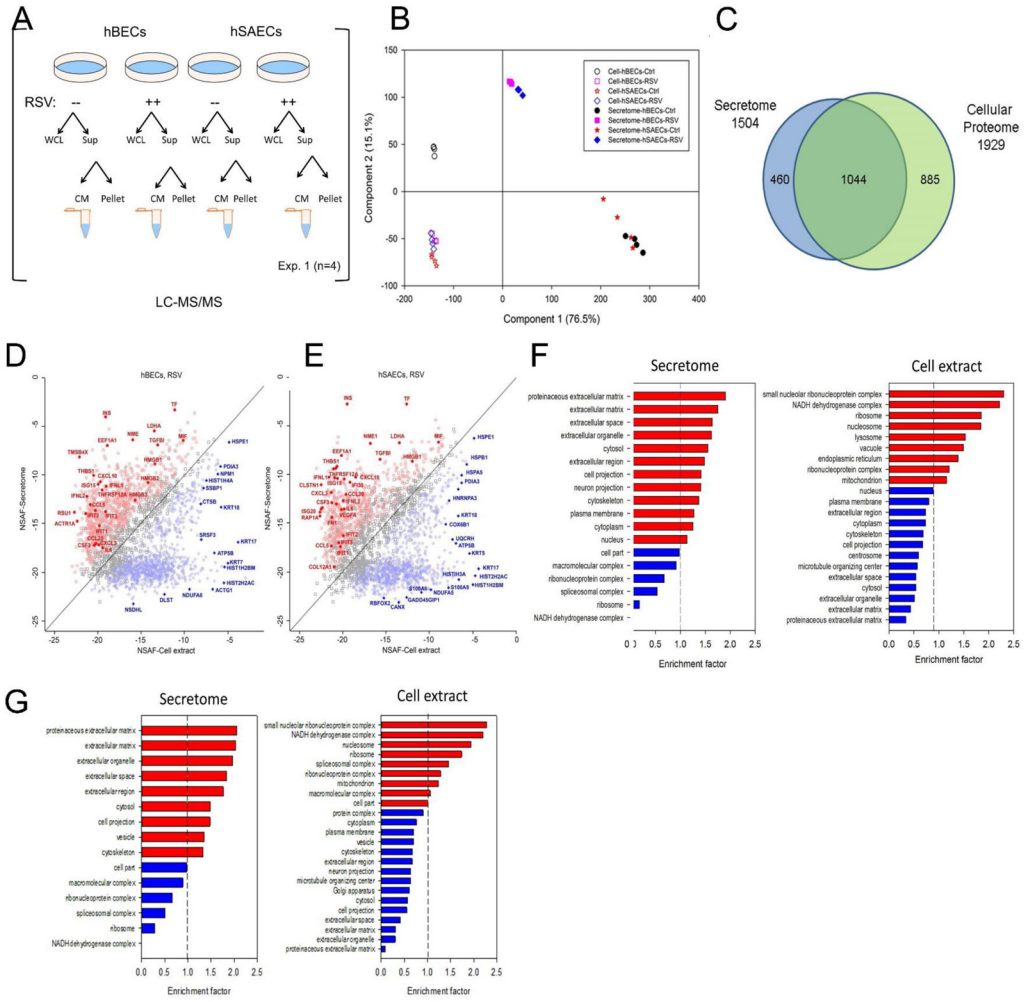

FIGURE 2.

Standardization of workflow for secretome characterization. **(A).** Schematic view of sample analysis by label-free LC-MS/MS. Four experiments were conducted on tert-hBECs and tert-hSAECs uninfected (control) or RSV-infected (MOI 1.0) for 24 h. Cell lysates and cell-free supernatants were isolated from each plate. Abbreviations: CM, conditioned medium; Exp, experiment; Sup, supernatant; WCL, whole-cell lysate. (**B).** The proteins from control- or RSV-induced secretome and whole cell lysates (WCLs) from tert-hBECs and tert-hSAECs were subjected to Principal Component Analysis (PCA). For each cell type and condition, the orthogonal transformation is applied. **(C).** Venn diagram showing the relationship between 1,929 WCL protein analysis vs the 1,504 proteins identified in both cell types. (**D**). Comparison of protein expression levels in the secretome vs that in WCLs for RSV-infected tert-hBECs. Normalized spectral abundance factor (NSAF) values of proteins identified in the tert-hBEC secretome (Y axis) were plotted vs their abundance in WCLs (X axis). Proteins in red are more enriched in the secretome (Benjamini Hochburg correct FDR <1%); proteins in blue are more enriched in WCLs. (**E**). Comparison of protein expression levels in the secretome vs that in WCLs for RSV-infected tert-hSAECs. NSAF values in the RSV-induced secretome (Y axis) are plotted vs their abundance in WCLs (X

axis). **(F).** GO Cellular Component enrichment (GOCC) of the tert-hBEC secretome and WCL (cell extract). X axis, genome ontology enrichment factor. Only GO classifications with FDR <1% are shown. Red bars indicate enrichment; blue bars indicate depletion. (**G**). GOCC of the tert-hSAEC secretome and WCL. Data are presented as in Fig. 2F.

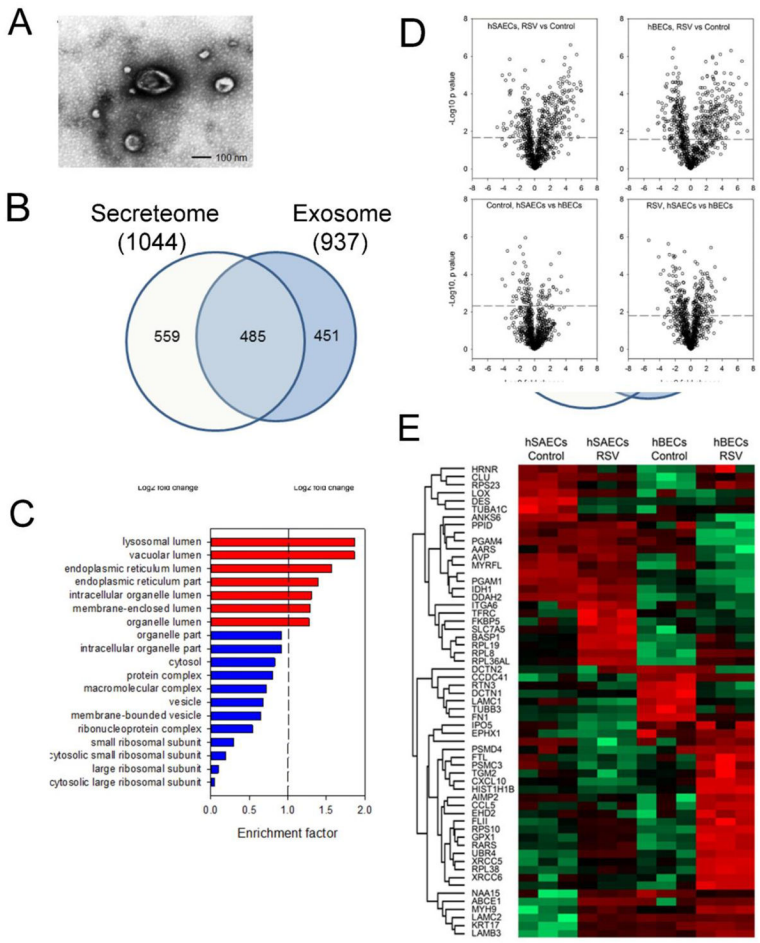

FIGURE 3.

Analysis of the exosomal fraction in the epithelial secretome. **(A).** Transmission electron microscopy of exosome fraction from tert-hSAECs. Note the membrane-enclosed vesicle, and characteristic “cupped” appearance. **(B)**. Overlap of exosomal and secretome protein identifications. Venn diagram of high- confidence proteins identified in each fraction. **(C).** GOCC of 937 identified exosomal proteins. X axis, genome ontology enrichment factor. Only GO classifications FDR <1% are shown. Red bars indicate enrichment; blue bars indicate depletion. **(D).** Volcano plots of pairwise comparison. The dashed lines indicate the Student’s *t*-test Benjamini-Hochberg FDR 5%; the dots above the dashed lines are proteins whose abundance was significantly changed. **(E).** 2-Dimensional hierarchical clustering of proteins whose abundance was significantly changed (Student’s *t*-test Benjamini-Hochberg FDR 5%, fold change > 5-fold). Expression values of proteins were z-score-normalized data of log2-transformed expression values for biological replicates. Hierarchical clustering was performed with columns representing cell samples and rows representing individual proteins (green, low expression, red, high expression). The protein name is given for each row.

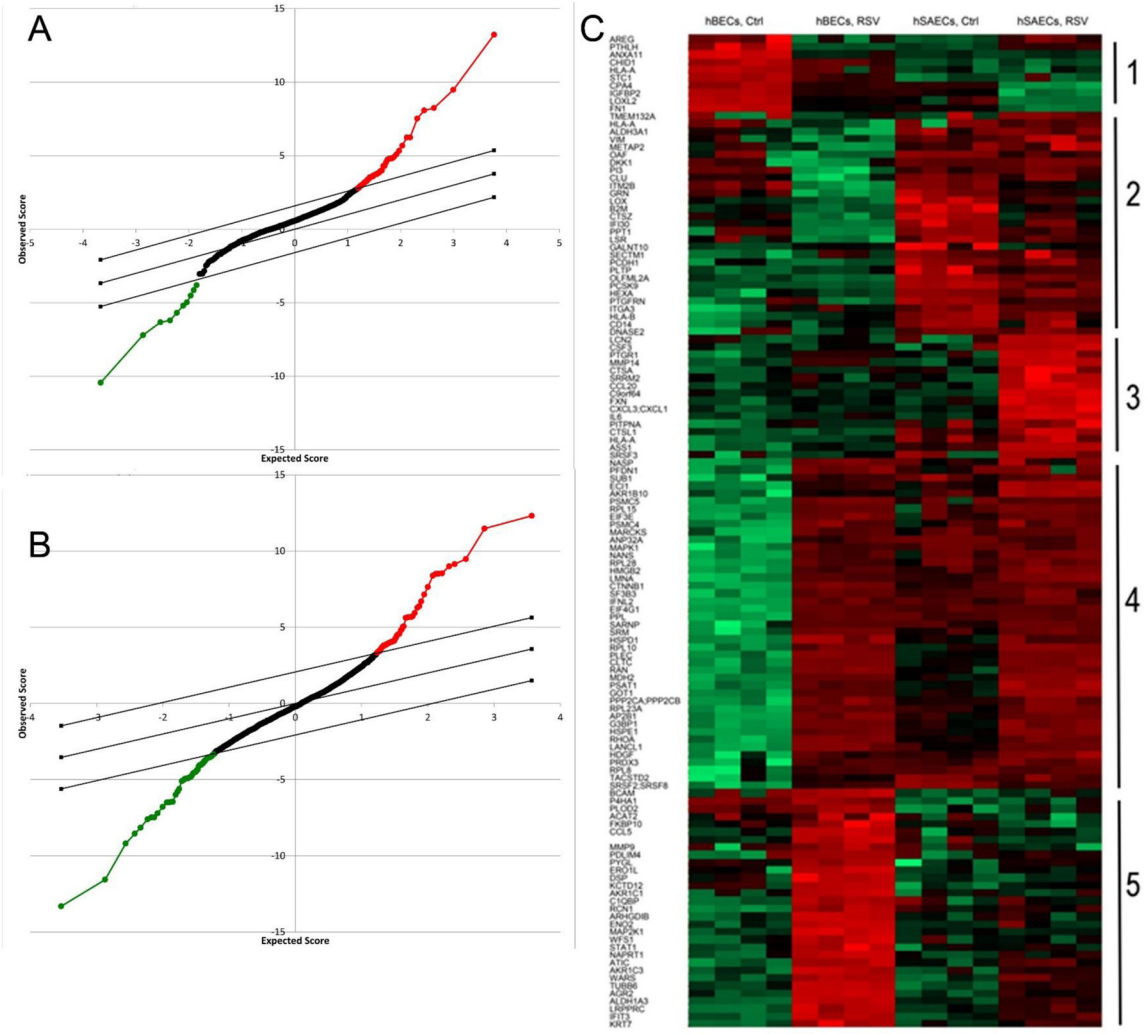

FIGURE 4.

Identification of differentially expressed proteins in the secretome of tert-hSAECs and tert-hBECs in response to RSV infection. **(A).** Statistical analysis of microarray (SAM) for secretome proteins whose expression differs by cell type in the basal state. X axis, expectation score; Y axis, observation score. The diagonal line shows where FDR = 0.01. Points above (in red) outside the threshold are those with FDR < 0.01, and points below the threshold (in green) are those proteins with FDR > 0.01. Proteins with increased expression in hSAECs are indicated by red points; those decreased are indicated in green. (**B**). SAM for secretome proteins whose expression differs due to RSV infection. (**C**). Expression values of proteins were z-score-normalized data of log2-transformed expression values for biological replicates. 2-dimensional hierarchical clustering was performed, with columns representing cell samples and rows representing individual proteins (green, low expression, red, high expression). The protein name is given for each column. The 5 major clusters are numbered at the right.

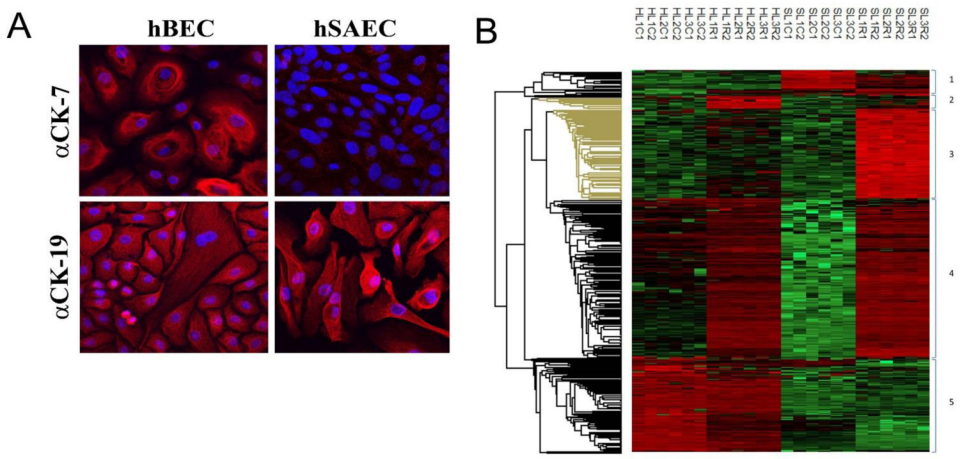

FIGURE 5.

Identification of differentially expressed proteins in primary airway epithelial cells. (**A**). Immunofluorescence of differential cytokeratin expression. phBECs or phSAECs plated on collagen coverslips were fixed and stained with anti-cytokeratin (CD)-7 or 19-selective Abs. Secondary detection was Alexa Fluor 568 (red)-conjugated goat anti-rabbit IgG. Nuclei were counterstained with DAPI and images acquired by confocal microscopy. For each antigen, the merged DAPI image is shown. **(B).** Hierarchical clustering of secretome proteins from primary airway cells. Differentially expressed proteins identified in the secretomes of primary phBECs and primary phSAECs through the analysis in Figs. 2–4 are shown. Log2-transformed expression values for biological replicates values were z-score-normalized and subjected to hierarchical clustering. Shown are individual data for each biological replicate. Abbreviations used are: H, phBECs; S, phSAECs; L#, lot number (different donors); C, control; R, RSV; Arabic numbering (1,2) indicates technical replicate.

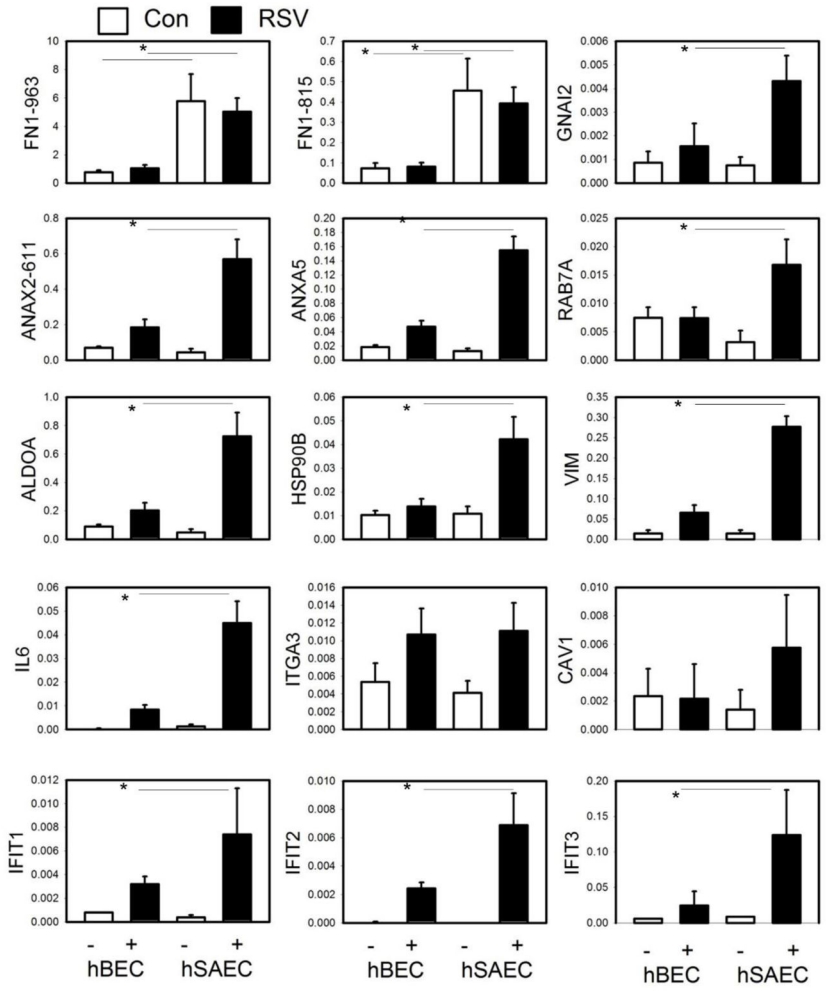

FIGURE 6.

Validation of differential expression of secretome proteins from primary airway cells. SID-SRM assays were performed for representative proteins in each cluster. For each protein, shown are the relative expression changes in secretome by cell type and the presence or absence of RSV infection.

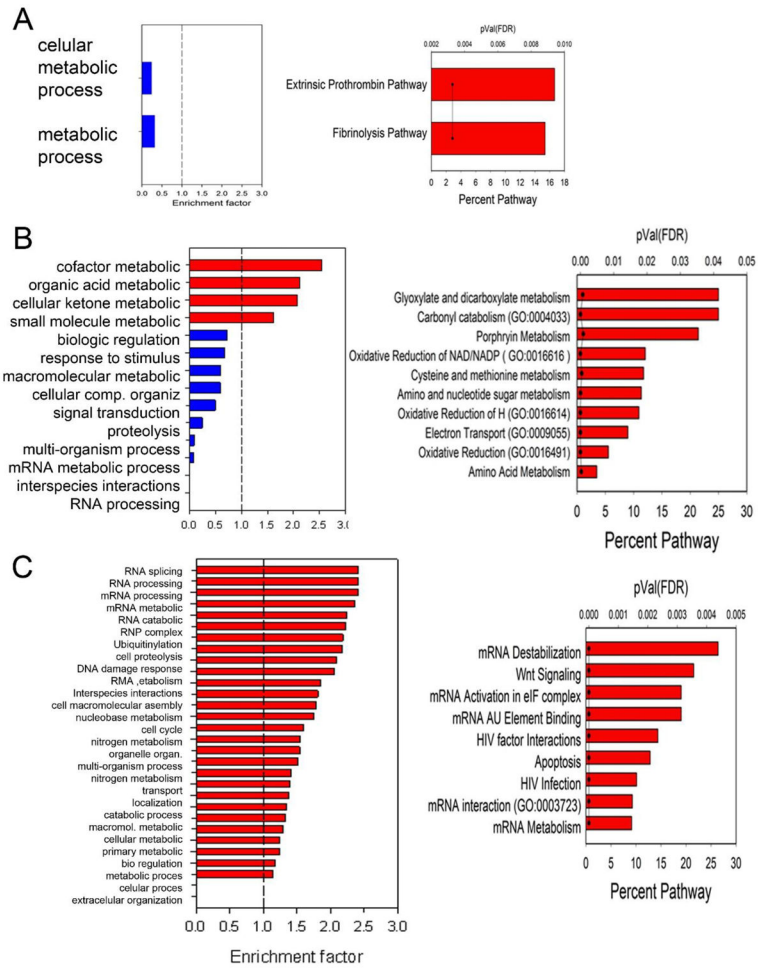

FIGURE 7.

Analysis of biological function. For each cluster in Fig. 5B, GO biological function enrichment and GeneSet enrichment analysis for canonical pathways was performed. (**A)** Cluster 2 analyses. Left panel, GO enrichment. X axis, enrichment factor; the dotted vertical line is the threshold for enrichment or depletion. Right panel, GSEA analysis for enrichment of canonical pathways. Percent of pathway indicates the number of proteins in the dataset that are matched to the pathway. pVal is the statistical significance of the enrichment by false discovery rate (FDR). (**B**). Cluster 3 analyses. Left, GO; right GSEA. (C). Cluster 4 analyses.

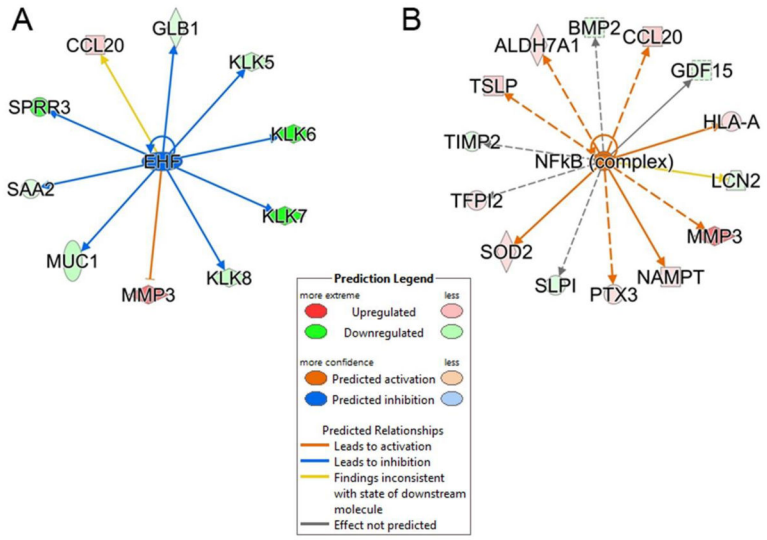

FIGURE 8.

Upstream Regulator Analysis. Upstream regulator analysis was conducted to determine transcription factors regulating the proteins in cluster 3. Shown are the overlap P-value measuring network enrichment and activation Z-score for each of two networks. (**A**). ETS homologous factor (EHF) network. Shown is a downregulated network (blue) with an activation Z-score of -2.53. Abbreviations: EHF, ets homologous factor; KLK, Kallikrein-like peptidase; SPRR3, small proline-rich protein 3; MUC, mucin; SAA, serum amyloid A. (**B**). Upregulated NFκB network. This network is activated by RSV with an activation Z score of +2.131. Abbreviations: BMP, bone morphogenic protein; MMP, matrix metalloproteinase; TIMP, metalloproteinase inhibitor; SOD, superoxide dismutase.

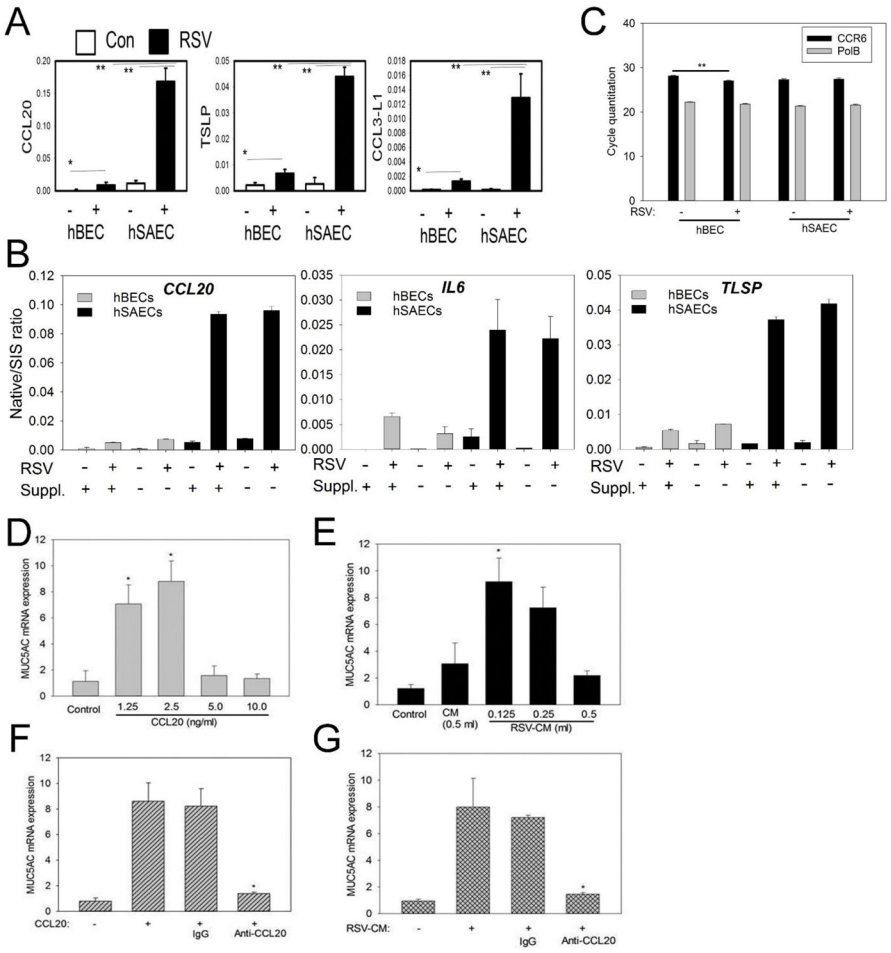

FIGURE 9.

Differential secretion of CCL20, TSLP and CCL-33. (**A**). SID-SRM for CCL20, TSLP and CCL-33 for phBECs vs phSAECs. Data are relative changes in expression in the secretome by RSV infection and cell type. (**B**). Differential expression is independent of the presence of medium supplements. SID-SRM for CCL20, TSLP, CCL-33 and IL-6 for phBECs and phSAECs grown and infected in the absence (−) or presence (+) of BSA/growth factor supplementation. Each bar is the mean ± SEM of triplicate determinations. (**C**). Cells were infected with or without RSV for 24h. Equal amounts of cDNA were taken for Q-RT-PCR for CCR6 and POLB expression using gene-specific primers. Each bar represents the mean ± SEM of cycle threshold (Ct) for triplicate assays. Experiments were repeated twice. ** = $p<0.004$. (**D**) Recombinant human CCL20 induces expression of mucin (MUC5AC) by hSAE cells *in vitro*. Different concentrations of recombinant CCL20 (rCCL20) were added to phSAEC cultures for 6 h. Shown is the fold change in MUC5AC mRNA expression by Q-RT-PCR. (**E**). hSAECs were incubated with different volumes of uninfected (CM) or UV-inactivated RSV conditioned medium (RSV-CM) for 6 h. MUC5AC mRNA expression was measured by Q-RT-PCR. (**F**). rCCL20 (2.5 ng/ml) was neutralized with mouse mAb to hCCL20 (25 ug/mL) or the same concentration of mouse IgG and added to the cell culture for 6 h. MUC5AC mRNA expression was assessed by Q-RT-PCR. (**G**). RSV-CM (0.125 ml)

was neutralized with anti-hCCL20 mAb (25 μg) in 1 ml of culture medium or the same amount of mouse IgG, added to the cell culture and incubated for 6 h. MUC5AC mRNA expression was assessed by Q-RT-PCR.

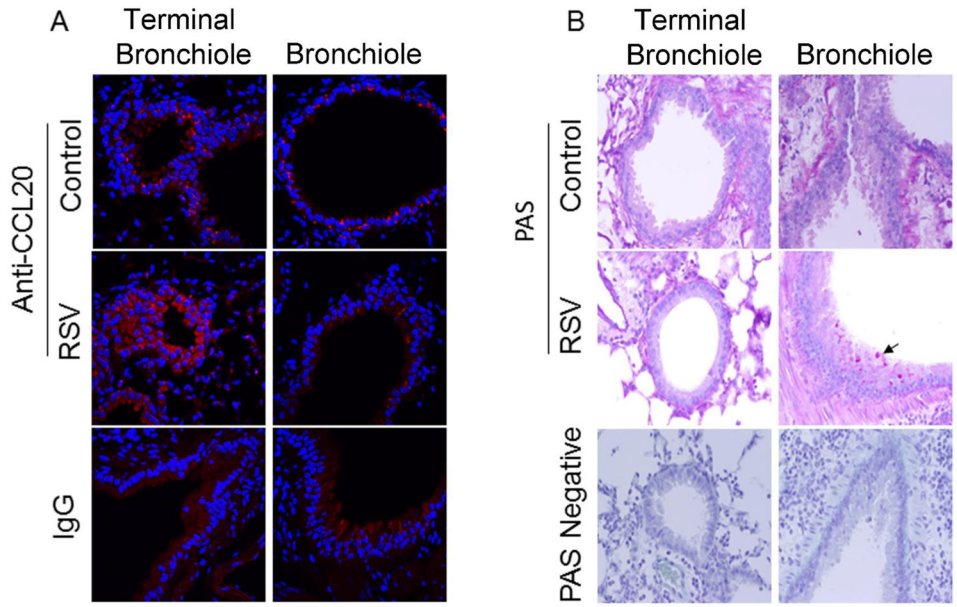

FIGURE 10. Expression of CCL20 and mucin production by airways of mice uninfected or infected with RSV

(**A**) Confocal microscopic images of distal airways (terminal bronchiole and bronchiole) showing CCL20 expression by immunofluorescence. Uninfected (Control) or RSV-infected (RSV) mouse lung sections were probed with anti-CCL20 antibody (anti-CCL20) or pre-immune serum (IgG). (**B**) Light microscopic images of distal lung sections subjected to Periodic Acid Schiff (PAS) reactions or without PAS.

Table I

Reproducibility of protein expression.

hBEC-Control	Replicate 1	Replicate 2	Replicate 3	Replicate 4
Replicate 1		0.876	0.865	0.861
Replicate 2	0.876		0.858	0.863
Replicate 3	0.865	0.858		0.852
Replicate 4	0.861	0.863	0.852	
Mean ± SD	0.863 ± 0.008			
hBEC-RSV	**Replicate 1**	**Replicate 2**	**Replicate 3**	**Replicate 4**
Replicate 1		0.955	0.959	0.95
Replicate 2	0.955		0.958	0.956
Replicate 3	0.959	0.958		0.966
Replicate 4	0.95	0.956	0.966	
Mean ± SD	0.957 ± 0.005			
hSAEC-Control	**Replicate 1**	**Replicate 2**	**Replicate 3**	**Replicate 4**
Replicate 1		0.866	0.86	0.859
Replicate 2	0.866		0.88	0.86
Replicate 3	0.86	0.88		0.851
Replicate 4	0.859	0.86	0.851	
Mean ± SD	0.863 ± 0.010			
hSAEC- RSV	**Replicate 1**	**Replicate 2**	**Replicate 3**	**Replicate 4**
Replicate 1		0.934	0.929	0.946
Replicate 2	0.934		0.952	0.929
Replicate 3	0.929	0.952		0.924
Replicate 4	0.946	0.929	0.924	
Mean ± SD	0.936 ± 0.011			

For each CM preparation shown is the Pearson's correlation coefficient (R^2) of the pairwise analysis of log2 protein abundance (NSAF; the log-log plots are shown in Supplementary Figure S1).

Table II

Differentially expressed proteins by cluster.

Cls	ID	Name	Cls	ID	Name	Cls	ID	Name	Cls	ID	Name	Cls	ID	Name	Cls	ID	Name
1	Q96JP9	CDHR1	3	P30519	HMOX2	4	P52823	STC1	4	Q9UKK9	NUDT5	4	P55884	EIF3B	5	Q8WVN6	SECTM1
1	Q29960	HLA-C	3	Q9P0L0	VAPA	4	Q99941	ATF6B	4	O15511	ARPC5	4	P26599	PTBP1	5	O43240	KLK10
1	P09871	C1S	3	P21399	ACO1	4	P06576	ATP5B	4	O95373	IPO7	4	P06748	NPM1	5	P06731	CEACAM5
1	O14817	TSPAN4	3	P09417	QDPR	4	O00754	MAN2B1	4	Q15366	PCBP2	4	O14980	XPO1	5	Q9Y337	KLK5
1	P41159	LEP	3	P23434	GCSH	4	P04080	CSTB	4	P53582	METAP1	4	O43776	NARS	5	P15941	MUC1
1	Q9P121	NTM;OPCML	3	P35270	SPR	4	P18510	IL1RN	4	Q13247	SRSF6	4	Q9UBQ5	EIF3K	5	Q05639	EEF1A2
1	Q8IUX7	AEBP1	3	Q92882	OSTF1	4	P20062	TCN2	4	Q13177	PAK2	4	P62318	SNRPD3	5	Q92876	KLK6
1	P01011	SERPINA3	3	O15347	HMGB3	4	P51610	HCFC1	4	Q14240	EIF4A2	4	Q16555	DPYSL2	5	Q96NY8	PVRL4
1	P20908	COL5A1	3	Q99798	ACO2	4	P16403	HIST1H1C	4	Q9BW04	SARG	4	P05388	RPLP0	5	Q9GZN4	PRSS22
1	P16189	HLA-A	3	Q9Y2D5	AKAP2	4	P62854	RPS26/11	4	Q9P1F3	ABRACL	4	Q16531	DDB1	5	B0FP48	UPK3BL
1	Q7Z406	MYH14	3	P58107	EPPK1	4	Q15181	PPA1	4	P49720	PSMB3	4	Q13263	TRIM28	5	Q99988	GDF15
1	O75487	GPC4	3	Q9NX46	ADPRHL2	4	P12004	PCNA	4	P55735	SEC13	4	Q03405	PLAUR	5	O00220	TNFRSF10A
1	P08254	MMP3	3	P04181	OAT	4	P20340	RAB6A/B	4	P84090	ERH	4	Q09028	RBBP4	5	Q6UXB2	CXCL17
1	P01344	IGF2	3	P50452	SERPINB8	4	Q15819	UBE2V2	4	P30419	NMT1	4	Q07955	SRSF1	5	P30455	HLA-A
1	Q9BY76	ANGPTL4	3	Q96EK6	GNPNAT1	4	P06454	PTMA	4	P14550	AKR1A1	4	P31943	HNRNPH1	5	Q14210	LY6D
1	O00469	PLOD2	3	Q969D9	TSLP	4	P51148	RAB5C	4	Q96KP4	CNDP2	4	O00231	PSMD11	5	P02533	KRT14
1	Q14766	LTBP1	3	Q8TEA8	DTD1	4	P46060	RANGAP1	4	P10809	HSPD1	4	P23588	EIF4B	5	Q14956	GPNMB
1	P26022	PTX3	3	Q5JRX3	PITRM1	4	Q13838	DDX39A/B	4	P84077	ARF1	4	P08621	SNRNP70	5	Q08431	MFGE8
1	P35442	THBS2	3	Q53FA7	TP53I3	4	P29966	MARCKS	4	P47895	ALDH1A3	4	Q9HB71	CACYBP	5	O75144	ICOSLG
1	P05090	APOD	3	P54105	CLNS1A	4	P54727	RAD23B	4	Q15056	EIF4H	4	P05023	ATP1A1	5	Q13510	ASAH1
1	P35573	AGL	3	O75884	RBBP9	4	O15144	ARPC2	4	Q9UL46	PSME2	4	P62195	PSMC5	5	Q13421	MSLN
1	P01009	SERPINA1	3	O95994	AGR2	4	P31153	MAT2A	4	Q15121	PEA15	4	O75821	EIF3G	5	Q86XX4	FRAS1
1	P02751	FN1	3	Q8NBJ7	SUMF2	4	Q12765	SCRN1	4	P53004	BLVRA	4	P38159	RBMX	5	P12273	PIP
1	Q8NES3	LFNG	3	P16619	CCL3L1	4	P55060	CSE1L	4	O60271	SPAG9	4	Q99536	VAT1	5	P25391	LAMA1
1	P48307	TFPI2	3	P52566	ARHGDIB	4	O95202	LETM1	4	P20290	BTF3	4	Q96AE4	FUBP1	5	Q6UVK1	CSPG4
1	Q00341	HDLBP	3	O60749	SNX2	4	P29508	SERPINB3	4	P53999	SUB1	4	P61088	UBE2N	5	Q6UWP8	SBSN
1	P05231	IL6	3	P36551	CPOX	4	Q16629	SRSF7	4	O43396	TXNL1	4	Q9NTK5	OLA1	5	O15031	PLXNB2

Cls	ID	Name	Cls	ID	Name	Cls	ID	Name	Cls	ID	Name	Cls	ID	Name	Cls	ID	Name
1	P09238	MMP10	3	Q9UFN0	NIPSNAP3A	4	P38606	ATP6V1A	4	Q9UHD1	CHORDC1	4	P40926	MDH2	5	Q13361	MFAP5
1	P32004	L1CAM	3	Q8WWM9	CYGB	4	Q13451	FKBP5	4	Q07666	KHDRBS1	4	P30048	PRDX3	5	P61812	TGFB2
1	Q96AY3	FKBP10	3	P04179	SOD2	4	P62263	RPS14	4	P35998	PSMC2	4	P35221	CTNNA1	5	Q09328	MGAT5
1	P30042	C21orf33	3	P67870	CSNK2B	4	Q15942	ZYX	4	Q01650	SLC7A5	4	P49419	ALDH7A1	5	P13929	ENO3
1	P63136	ERVK-6/18/19/25	3	O60701	UGDH	4	P20073	ANXA7	4	Q13185	CBX3	4	P48739	PITPNB	5	P98095	FBLN2
1	Q9UK41	VPS28	3	P30084	ECHS1	4	Q01581	HMGCS1	4	O60218	AKR1B10	4	Q9NR45	NANS	5	Q68BL7	OLFML2A
			3	P13804	ETFA	4	Q92688	ANP32B	4	P21281	ATP6V1B2	4	Q9Y3A5	SBDS	5	P16870	CPE
2	Q9UM73	ICAM5	3	O15305	PMM2	4	Q06323	PSME1	4	Q16222	UAP1	5	Q99523	SORT1	5	P13686	ACP5
2	O14791	HS3ST1	3	O76054	SEC14L2	4	P12956	XRCC6	4	P51149	RAB7A	5	Q6UW49	SPESP1	5	Q9UI42	CPA4
2	Q01638	IL1RL1	3	P49411	TUFM	4	Q02790	FKBP4	4	O43765	SGTA	5	O75367	H2AFY	5	P12109	COL6A1
2	Q29980	MICB	3	Q5T2P8	ANXA8L1	4	Q13404	UBE2V1	4	P62266	RPS23	5	Q5D862	FLG2	5	O75976	CPD
2	P30499	HLA-C	3	Q16836	HADH	4	P63208	SKP1	4	P17980	PSMC3	5	O60353	FZD6	5	P07225	PROS1
2	P05204	HMGN2/3	3	Q9Y4K1	AIM1	4	Q13765	NACA	4	Q9UK22	FBXO2	5	A1L020	MEX3A	5	P09668	CTSH
2	P17693	HLA-G	3	Q9HD15	SRA1	4	P36871	PGM1	4	P12268	IMPDH2	5	P03952	KLKB1	5	P16035	TIMP2
2	Q9NQC3	RTN4	3	Q59GN2	RPL39P5	4	P28070	PSMB4	4	Q14203	DCTN1	5	Q9GZM5	YIPF3	5	Q9NPC4	A4GALT
2	Q96QD8	SLC38A2	3	O15400	STX7	4	Q5VT79	ANXA8L2	4	P61019	RAB2A;RAB2B	5	Q9NPH3	IL1RAP	5	P23471	PTPRZ1
2	P12643	BMP2	3	P31146	CORO1A	4	P10314	HLA-A	4	Q99733	NAP1L4	5	Q8NCC3	PLA2G15	5	Q9UIV8	SERPINB13
2	P25205	MCM3	3	Q13642	FHL1	4	O95571	ETHE1	4	Q7L576;Q96F07	CYFIP1;CYFIP2	5	Q9BZG9	LYNX1	5	Q641Q3	METRNL
			3	Q9H993	C6orf211	4	P05091	ALDH2	4	O14818	PSMA7	5	Q86YZ3	HRNR	5	P0DJI9	SAA2
3	Q13509	TUBB3	3	Q15149	PLEC	4	Q5TZA2	CROCC	4	P41227	NAA10	5	O00748	CES2	5	Q5SYB0	FRMPD1
3	Q9Y570	PPME1	3	P35754	GLRX	4	P38571	LIPA	4	P07910	HNRNPC	5	P24593	IGFBP5	5	Q08174	PCDH1
3	P07738	BPGM	3	Q01995	TAGLN	4	O14745	SLC9A3R1	4	Q9UMX0	UBQLN1	5	Q9Y653	GPR56	5	P32926	DSG3
3	P61081	UBE2M	3	P48745	NOV	4	P63098	PPP3R1	4	P49588	AARS	5	Q92997	DVL3	5	P03973	SLPI
3	P56211	ARPP19	3	O00244	ATOX1	4	Q9H0E2	TOLLIP	4	P62277	RPS13	5	O95428	PAPLN	5	Q6E0U4	DMKN
3	Q9BV57	ADI1	3	P26885	FKBP2	4	P49721	PSMB2	4	P63167	DYNLL1	5	P52798	EFNA4	5	O75635	SERPINB7
3	Q9H8S9	MOB1A/B	3	P06132	UROD	4	P17066	HSPA6	4	Q04637	EIF4G1	5	P25774	CTSS	5	Q9Y5Y6	ST14
3	P50583	NUDT2	3	P37268	FDFT1	4	P25789	PSMA4	4	P67809	YBX1	5	Q6PCB0	VWA1	5	O95274	LYPD3
3	P99999	CYCS	3	Q08257	CRYZ	4	O76003	GLRX3	4	O60763	USO1	5	O75054	IGSF3	5	Q99519	NEU1
3	P42126	ECI1	3	Q8NFU3	TSTD1	4	P00918	CA2	4	P52895	AKR1C2	5	P21217	FUT3	5	Q16610	ECM1

Cls	ID	Name	Cls	ID	Name	Cls	ID	Name	Cls	ID	Name	Cls	ID	Name	Cls	ID	Name
3	Q9P2F8	SIPA1L2	3	Q9NQR4	NIT2	4	Q01130	SRSF2	4	P52788	SMS	5	P20800	EDN2	5	P07339	CTSD
3	A6NDG6	PGP	3	P30838	ALDH3A1	4	P15924	DSP	4	P05198	EIF2S1	5	Q9NY97	B3GNT2	5	P80188	LCN2
3	Q1KMD3	HNRNPUL2	3	P78556	CCL20	4	P30740	SERPINB1	4	P43686	PSMC4	5	Q9BUD6	SPON2	5	Q9NQ38	SPINK5
3	Q86TI2	DPP9	3	O95394	PGM3	4	Q16831	UPP1	4	Q99729	HNRNPAB	5	P29373	CRABP2	5	P49862	KLK7
3	P25325	MPST	3	Q9ULC4	MCTS1	4	P46783	RPS10	4	Q7L1Q6	BZW1	5	P00352	ALDH1A1	5	Q9UBC9	SPRR3
3	O43813	LANCL1	3	P12532	CKMT1A	4	P52597	HNRNPF	4	Q15370	TCEB2	5	P22528	SPRR1B	5	A8K2U0	A2ML1
3	P40261	NNMT	3	Q6FI81	CIAPIN1	4	Q96S86	HAPLN3	4	Q9Y617	PSAT1	5	P54652	HSPA2	5	P06396	GSN
3	Q00169	PITPNA	3	P42330	AKR1C3	4	P50995	ANXA11	4	Q99873	PRMT1	5	P42785	PRCP	5	Q9UMX5	NENF
3	P61086	UBE2K	3	Q13011	ECH1	4	Q15847	ADIRF	4	P22626	HNRNPA2B1	5	P10619	CTSA	5	P17096	HMGA1
3	Q13126	MTAP	3	P51572	BCAP31	4	P08133	ANXA6	4	P11940	PABPC1	5	Q14563	SEMA3A	5	Q9NZ08	ERAP1
3	P10768	ESD	3	O75390	CS	4	P48163	ME1	4	O75223	GGCT	5	O95490	LPHN2			
3	P50479	PDLIM4	3	P30520	ADSS	4	P07384	CAPN1	4	Q92841	DDX17	5	Q00888	PSG4			
3	P82979	SARNP	3	Q9NQ88	TIGAR	4	P35222	CTNNB1	4	Q92499	DDX1	5	Q9HB40	SCPEP1			
3	P27144	AK4	3	Q9H2U2	PPA2	4	P27695	APEX1	4	P31939	ATIC	5	Q07954	LRP1			
3	Q9BY32	ITPA	3	Q15833	STXBP2	4	Q9H3K6	BOLA2	4	P38646	HSPA9	5	Q99102	MUC4			
3	P48637	GSS	3	P21266	GSTM3	4	P07203	GPX1	4	Q9H6S3	EPS8L2	5	Q9UN76	SLC6A14			
3	Q9GZP4	PITHD1	3	O75368	SH3BGRL	4	O95777	LSM8	4	P15170	GSPT1	5	P60022	DEFB1			
3	Q9NZD2	GLTP	3	P43490	NAMPT	4	Q9BVG4	PBDC1	4	P62269	RPS18	5	O00115	DNASE2			
3	Q05397	PTK2	3	Q8WUP2	FBLIM1	4	P14923	JUP	4			5	Q99715	COL12A1			
3	P52943	CRIP2	3	P19623	SRM	4	P22102	GART	4	Q96QK1	VPS35	5	P16278	GLB1			
3	P42771	CDKN2A	3	Q9HAV7	GRPEL1	4	P05455	SSB	4	Q15019	SEPTIN2	5	O60259	KLK8			
			3	P29218	IMPA1	4	P00568	AK1	4	O75436	VPS26A	5	P58062	SPINK7			
			3	P34897	SHMT2	4	P35080	PFN2	4	P14866	HNRNPL	5	P15586	GNS			
			3	Q9BSJ8	ESYT1	4	Q8WUW1	BRK1	4	Q92973	TNPO1	5	P20061	TCN1			
			3	P23368	ME2	4	Q9Y383	LUC7L2	4	Q14152	EIF3A	5	Q9UBX7	KLK11			
			3	P42704	LRPPRC	4	P30044	PRDX5	4	Q13442	PDAP1	5	Q14CN2	CLCA4			
			3	O15231	ZNF185				4	Q13151	HNRNPA0	5	Q9H7M9	C10orf54			
			3	Q13630	TSTA3				4	P62495	ETF1	5	P01833	PIGR			
			3	O00515	LAD1							5	P36543	ATP6V1E1			

Cls	ID	Name	Cls	ID	Name	Cls	ID	Name	Cls	ID	Name	Cls	ID	Name	Cls	ID	Name
												5	Q9Y2A9	B3GNT3			
												5	Q8WXI7	MUC16			
												5	O43653	PSCA			
												5	Q14508	WFDC2			

For each cluster (Cls) shown in Fig. are listed the protein ID and name.